Acta Pharmaceutica Sinica B 2026;16(5):2982−3000

Chinese Pharmaceutical Association
Institute of Materia Medica, Chinese Academy of Medical Sciences

Acta Pharmaceutica Sinica B

www.elsevier.com/locate/apsb
www.sciencedirect.com

ORIGINAL ARTICLE

CD74 deficiency protects against doxorubicin cardiotoxicity through RRM2-mediated regulation of ferroptosis

Miyesaier Abudureyimu[a,†], Guizhen Wang[b,c,†], Xing Qin[d,†], Peizhi Miao[a], Jie Qi[e], Richard Bucala[f], Rong Chen[g], Junbo Ge[h,i,j,k], Yingmei Zhang[h,i,j,k,*], Xuanming Luo[l,*], Jun Ren[h,i,j,k,*]

[a]*Cardiovascular Department, Shanghai Xuhui Central Hospital, Fudan University, Shanghai 200031, China*
[b]*Department of Emergency, Shanghai Tenth People's Hospital, School of Medicine Tongji University, Shanghai 200072, China*
[c]*Department of Critical Care Medicine, Shanghai Pulmonary Hospital, Tongji University, Shanghai 200433, China*
[d]*Department of Cardiology, Xijing Hospital, Air Force Medical University, Xi'an 710032, China*
[e]*School of Pharmaceutical Sciences, Wenzhou Medical University, Wenzhou 325035, China*
[f]*Department of Medicine, Yale School of Medicine, New Haven, CT 06520, USA*
[g]*Department of Pharmacy, The First Affiliated Hospital of Soochow University, Suzhou 215006, China*
[h]*Department of Cardiology, Zhongshan Hospital, Fudan University, Shanghai Institute of Cardiovascular Diseases, Shanghai 200032, China*
[i]*Key Laboratory of Viral Heart Diseases, National Health Commission, Shanghai 200032, China*
[j]*Key Laboratory of Viral Heart Diseases, Chinese Academy of Medical Sciences, Shanghai 200032, China*
[k]*National Clinical Research Center for Interventional Medicine, Shanghai 200032, China*
[l]*Department of General Surgery, Shanghai Xuhui Central Hospital, Fudan University, Shanghai 200031, China*

Received 30 August 2025; received in revised form 21 November 2025; accepted 22 December 2025

KEY WORDS

CD74;
Doxorubicin;
Cardiotoxicity;
Mitochondrial integrity;

Abstract Doxorubicin (DOX)-induced cardiotoxicity (DIC) is a major health threat that limits its clinical application. While mitochondrial dysfunction, oxidative stress and ferroptosis are implicated in DIC pathology, the precise mechanism remains elusive. This study evaluated the role of cluster of differentiation 74 (CD74), an immunoregulatory protein, in DIC. Our findings revealed elevated CD74 levels in blood samples from DOX-exposed patients and DOX-challenged mouse hearts. CD74 deletion mitigated

*Corresponding authors.
E-mail addresses: ren.jun@zs-hospital.sh.cn (Jun Ren), xuanmingluo@163.com (Xuanming Luo), zhang.yingmei@z-hospital.sh.cn (Yingmei Zhang).
†These authors made equal contributions to this work.

Peer review under the responsibility of Chinese Pharmaceutical Association and Institute of Materia Medica, Chinese Academy of Medical Sciences.

https://doi.org/10.1016/j.apsb.2026.01.028

Ferroptosis;
Oxidative stress;
Amifostine

DOX-indued cardiac remodeling, contractile anomaly, mitochondrial abnormalities, apoptosis, and ferroptosis. Mechanistically, CD74 bound to DNA synthesis molecule ribonucleotide reductase M2 (RRM2), redistributing it from cytoplasm to plasma membrane, impairing DOX-induced repair and exacerbating mitochondrial injury, apoptosis, and ferroptosis *via* activation of RRM2/p53 cascade. Notably, a CD74 mutant (aa 220−250) failed to aggravate DOX-induced cardiac dysfunction, unlike WT CD74. Moreover, the protective effects of CD74 inhibition in cardiomyocytes were negated by p53 activation, highlighting its role in DOX-induced damage. Treatment with CD74 inhibitor Amifostine in a DIC mouse model significantly alleviated cardiac remodeling and functional impairment by reducing oxidative stress and ferroptosis. Transwell study using the CD74-null Raw 264.7 macrophages and cardiomyocytes revealed that CD74 knockdown in macrophages overly attenuated DOX-instigated cardiomyocyte dysfunction. These findings establish CD74 as a potential therapeutic target for DIC, as its regulation of RRM2 cytomembrane diversion and ferroptosis ultimately drives cardiac remodeling and contractile anomalies in response to DOX challenge.

1. Introduction

Doxorubicin (DOX) and its derivative epirubicin are employed in the therapeutics of breast cancer, endometrial cancer, gastric cancer, pediatric solid tumors, soft tissue sarcomas, and aggressive lymphocytic or myelocytic leukemia[1]. However, clinical application of DOX has been greatly hampered by its toxicities including hematopoietic suppression, nausea, vomiting, extravasation, and alopecia, with cardiotoxicity being the most severe and life-threatening side-effect[2]. Of note, DOX-evoked cardiotoxicity is often progressive and irreversible, prompting development of cardiomyopathy in a dose-dependent manner. It was indicated that cardiotoxicity may occur at low doses likely due to the higher individual susceptibility[3,4]. To date, a number of scenarios have been postulated for the pathogenesis of DOX cardiomyopathy including DNA damage, mitochondrial injury, oxidative stress, inflammation, transcriptome alterations, and various forms of cardiomyocyte death[5-7]. Nonetheless, precise mechanisms behind DOX cardiotoxicity appear to be complex and multifactorial, making early monitoring and active prevention of DOX cardiotoxicity rather challenging.

Recent evidence has indicated a vital role for ferroptosis in DOX-induced heart damage. DOX can provoke ferroptosis through multiple machineries[8,9]. Fang and colleagues reported that DOX triggers ferroptosis by promoting nuclear factor erythroid 2-related factor 2 (Nrf2)-mediated upregulation of heme oxygenase-1 (Hmox1), which catalyzes heme degradation, leading to accumulation of non-heme iron and cytotoxicity[10]. In addition, Tadokoro and associates showed that DOX evokes ferroptosis in the mitochondria through down-regulation of glutathione peroxidase 4 (GPX4). Results in cardiomyocytes also demonstrated that GPX4 overexpression, or iron chelation targeting Fe^{2+} in mitochondria may effectively prevent DOX-induced ferroptosis, revealing a unique role for mitochondria as a primary target for DOX-instigated ferroptosis[11,12]. Meanwhile, mitochondrial damage, such as impaired bioenergetics, collapsed mitochondrial membrane potential, and increased ROS production, represents a hallmark for DOX cardiomyopathy[8,9]. In particular, recent evidence denoted a role for mitochondria-dependent ferroptosis in the etiology of DOX cardiomyopathy, although limited information is available with regards to the interplay between mitochondrial regulation and ferroptosis in DOX cardiomyopathy.

Cluster of Differentiation 74 (CD74) is a multifunctional transmembrane protein, primarily expressed in antigen-presenting cells (APCs) where it serves as a chaperone and surface receptor[11]. It plays a crucial role in the immune system by facilitating major histocompatibility complex class II (MHC-II) antigen presentation, ensuring efficient T cell activation[13]. Additionally, CD74 acts as a receptor for pathogens and antigens, enhancing their uptake by APCs and stabilizing MHC-II-antigen interactions[14]. Beyond antigen presentation, CD74 binds macrophage migration inhibitory factor (MIF), modulating inflammatory responses and apoptosis *via* p53 and NRF2 pathways[15,16]. Its dysregulation is linked to autoimmune diseases, inflammation, atherosclerosis, Alzheimer's disease, breast cancer, and diabetes mellitus[17,18], with upregulated expression in various pathological conditions. In summary, CD74 plays diverse, context-dependent roles, influencing immune regulation, inflammation, and cellular homeostasis. Its dual functions as an MHC-II chaperone and MIF receptor underscore its importance in both physiological and pathological processes[19,20]. Earlier studies indicated that DOX provokes cardiac iron deposit, accumulation of lipid peroxides, and cardiomyocyte ferroptosis, prompting mitochondrial injury and cardiac dysfunction[21]. In particular, DOX downregulates glutathione peroxidase 4 (GPX4), a critical enzyme detoxifying peroxidized lipids, resulting in overwhelmed lipid peroxidation and ferroptosis[22,23]. Here in this study, we evaluated the possible effect of CD74 ablation and inhibition on DOX cardiomyopathy and cell signaling mechanism involved with a special focus on ferroptosis.

2. Material and methods

2.1. Experimental animal and human plasma

The experimental procedures used in this work were approved by the Institutional Animal Use and Care Committees of Zhongshan Hospital (No. 2023-03-04, Shanghai, China) and were in accordance with the NIH Guideline. To establish a chronic DIC model, 8-week-old male CD74 knockout ($CD74^{-/-}$) and littermate WT mice received DOX (5 mg/kg, CAS No: 23214-92-8, MCE) or saline *via* intraperitoneal injection once weekly for 4 weeks[24,25]. For CD74 inhibition using Amifostine (CAS No.: 20537-88-6,

MCE), control and DIC mice were treated with Amifostine (80 mg/kg, dissolved in 10% DMSO and 90% saline, i.p.) once daily for 1 week[26]. Cardiac function was evaluated 1 week after the final DOX injection using echocardiography, followed by biochemical assays on collected heart tissues.

To measure blood levels of CD74, blood samples were obtained from breast cancer patients with clear indication of cardiac toxicity [DIC *vs.* non-DIC, age: 48.6 ± 4.6 year *vs.* 46.5 ± 5.3 year, $P > 0.05$; left ventricular ejection fraction (LVEF): 51.3 ± 4.9% *vs.* 64.7 ± 4.9%, $P < 0.05$; NT pro BNP: 189.7 ± 79.6 pg/mL *vs.* 29.9 ± 3.4 pg/mL, $P < 0.01$; $n = 12$] patients. Serum levels of CD74 and cardiac troponin-T (cTnT) were determined using commercial ELISA kits from BioVision (Mountain View, CA, USA) and Beyotime (Nanjing, China), respectively. The collection of serum from breast cancer patients receiving DOX therapy was approved by the Ethics Committee of Xuhui District Central Hospital Affiliated to Fudan University, and written informed consent was obtained from all participants. (Shanghai, China, No. 2024027).

2.2. Echocardiographic assessment

Mice were anesthetized by isoflurane (1.5%−3.0%) prior to cardiac assessment using a 2-D guided M-mode echocardiography (Vevo 2100, Visualsonics, Toronto, ON, Canada). Fractional shortening (FS) was calculated from LV end-diastolic (LVEDD) and LV end-systolic diameters (LVESD) using the equation of (LVEDD-LVESD)/LVEDD. Ejection fraction (EF) and heart rate (HR) were calculated using a Vevo 2100 echocardiography. For echocardiogram acquisition in temperature-controlled conditions, isoflurane was reduced to 1.0%−1.5% and was adjusted to maintain the heart rate within a range of 450−550 beats per min.

2.3. Single-cell sequencing and data analysis

GSE 205551 single-cell sequencing data were used to evaluate DOX's effect on the tumor immune microenvironment. To model the tumor microenvironment, syngeneic allografts were generated by injecting 4T1 cells (a breast cancer cell line) into the mammary fat pad of immune-competent BALB/c mice. When tumors reached ∼100 mm^3, mice received 5 mg DOX over seven days. Two days after the final dose, tumors were measured and CD45-sorted immune cells were enriched for single-cell sequencing[27]. By Day 8, tumors in the saline group expanded 400%, whereas DOX-treated tumor growth was either inhibited (sensitive) or unchanged (resistant). To analyze batch effects, Harmony (version 1.2.0) was employed. Principal component analysis (PCA) was used for linear dimension reduction, and Seurat2 standard pipeline processed single cell data, with cell annotation performed using R-package SingleR3. FeaturePlot, and ggplot2 library (https://github.com/tidyverse/ggplot2) were used for visualization. Clusters were identified *via* FindNeighbors and FindClusters in Seurat, while UMAP and t-SNE were performed using 'RunTSNE'. Cluster annotation relied on canonical cell markers and reference datasets for tumor cells. Differential analyses of various components were conducted using FinkMarkers, with results visualized *via* Enhanced Volcano plots (https://github.com/kevinblighe/EnhancedVolcano). Pathway analysis of Gene Ontology (GO), Kyoto Encyclopedia of Genes and Genomes (KEGG), and reactome were performed using clusterProfiler, while gene set variation analysis (GSVA) calculated gene set enrichment scores using the GSVA R package, generating an enrichment score matrix for each sample.

2.4. Transcriptomics and enrichment analysis

GSE 244574 and GSE224157 databases were analyzed to assemble transcriptomes and identify differentially expressed genes (DEGs). GSE244574 contains transcriptomic data from MCF7 breast cancer cells treated with DOX[28], while GSE224157 includes heart samples from DOX-treated and untreated mice analyzed *via* RNA-seq[29]. DESeq2 was used for differential expression analysis, with DEGs identified based on fold-change ≥ 2 and $P < 0.01$. Gene Ontology terms and KEGG pathways were used for functional analysis. Data visualization included volcano plots generated with ggplot and bubble plots for enrichment results using the ggplot R package.

2.5. Immunofluorescence and confocal imaging assay

Immunofluorescence staining for CD74/CD68/cTnT/CD3 was performed according to the manufacturer's instruction. Mouse heart slices from saline and DOX groups were fixed and permeabilized at room temperature, followed by blocking for 1 h. Samples were then incubated overnight at 4 °C with anti-CD74 (1:100), anti-cTnT (1:100), mouse anti-CD68 (1:100) and anti-CD3 (1:100) antibodies. After incubation, samples were incubated with anti-rabbit Alexa Fluor 488 (1:200) secondary antibodies for 1 h in the dark. Immunofluorescence was examined using a Leica SP8 laser confocal microscope (630 × oil objective, Weztlar, Germany) and images were analyzed using ImageJ[30].

2.6. RAW 264.7 macrophages

RAW 264.7 macrophages were purchased from Pricella (Wuhan, China). Cells were Transwell (0.4 μmol/L) co-cultured at a ratio of 1:20 (RAW 264.7 macrophages to adult mouse cardiomyocytes, AMCMs)[31].

2.7. Isolation and culture of AMCMs

To isolate AMCMs, mice were anesthetized, and a rapid thoracotomy was performed to expose the heart. The descending aorta was ligated, and 7 mL of EDTA buffer (Gibco) was injected into the right ventricle (RV) for immediate perfusion before transferring the heart to a 60-mm dish with fresh EDTA buffer. Digestion was initiated by sequentially injecting 10 mL of EDTA buffer, 3 mL of perfusion buffer, and 30−50 mL of collagenase buffer into the left ventricle (LV), followed by gentle trituration to achieve cellular dissociation, which was halted by adding 5 mL of stop buffer. The suspension was filtered through a 100-μm strainer and subjected to four rounds of gravity settling, while calcium concentration was gradually restored using three intermediate buffers. A yield of at least 80% rod-shaped AMCMs indicated successful isolation, after which cells were plated on laminin (5 μg/mL)-coated dishes at an appropriate density and maintained in an incubator at 37 °C with 5% CO_2[32].

To assess the possible effects of DOX, AMCMs were exposed to DOX (1 μmol/L) for 24 h before cell harvest, while control groups received saline for same duration[33]. To discern the impact of Amifostine on DOX-evoked cardiotoxicity, AMCMs were challenged by DOX or Amifostine (10 μmol/L) *in vitro* for 24 h. To evaluate the involvement of ferroptosis, AMCMs were

supplemented with the ferroptosis inhibitor Liproxstatin-1 (200 nmol/L, CAS No: 950455-15-9, MCE)[34], the p53 inhibitor Pifithrin-β (10 μmol/L, CAS No: 511296-88-1, MCE)[35], the p53 activator Kevetrin (80 mol/L, CAS No: 66592-89-0, MCE)[36], or the RRM2 inhibitor GW8510 (4 μmol/L, CAS No: 222036-17-1, MCE)[37] prior to assessment of lipid peroxidation and contractile properties.

2.8. *Histological examination*

Following anesthesia with ketamine (80 mg/kg; Pfizer, Berlin, Germany) and xylazine (12 mg/kg; Bayer AG, Leverkusen, Germany), mice were sacrificed, and hearts were excised and immediately placed in 10% neutral-buffered formalin at room temperature for 24 h. After fixation in 4% paraformaldehyde, heart tissues were paraffin-embedded and sectioned cross-sectionally (5 μm-thick), deparaffinized and rehydrated. Hematoxylin and eosin (H&E) staining was used for general morphology assessment. Alexa Fluor 488-labeled wheat germ agglutinin (WGA) lectin staining and H&E staining are shown in Fig. 3, and H&E staining is also presented in Fig. 8, were employed to evaluate myocardial atrophy. Masson trichrome staining was employed to detect fibrosis. For oxidative stress assessment, myocardial slices were incubated overnight to anti-4-hydroxynonenal (4-HNE, 1:100, Cat No. ab46545, Abcam) antibody, followed by secondary antibody incubation. Cardiomyocyte cross-sectional areas were measured using a digital microscope (400 ×) with ImageJ software (version2.3.0, NIH), excluding cells with incomplete edges or extreme roundness indices. Percentage of fibrosis was quantified using the Adobe Photoshop software (Adobe Systems Inc, San Jose, CA, USA), with light blue-stained area normalized to the total area. The quantitation of 4-HNE positive areas (brown or brownish staining) in heart slices was performed using a digital microscope (400 ×).

2.9. *Detection of reactive oxygen species (ROS) and TUNEL*

Myocardial tissue slices were rinsed with pre-warmed 37 °C PBS, and AMCMs were incubated with 10 μmol/L DCFH-DA (avoid exposure to light) fluorescence probe (Beyotime, China, diluted 1:1000 in serum-free medium) for 20 min at 37 °C. Cells were then washed three times with PBS. DCFH-DA was excited at 488 nm and emitted at 525 nm, with detection performed immediately post-staining. ROS fluorescence intensity was quantified using ImageJ software. For apoptosis assessment, TUNEL assay was conducted using the One Step TUNEL Apoptosis Assay Kit (Beyotime S1086, China). Frozen heart slices were incubated with TUNEL solution for 1 h prior to fluorescent imaging using a Leica

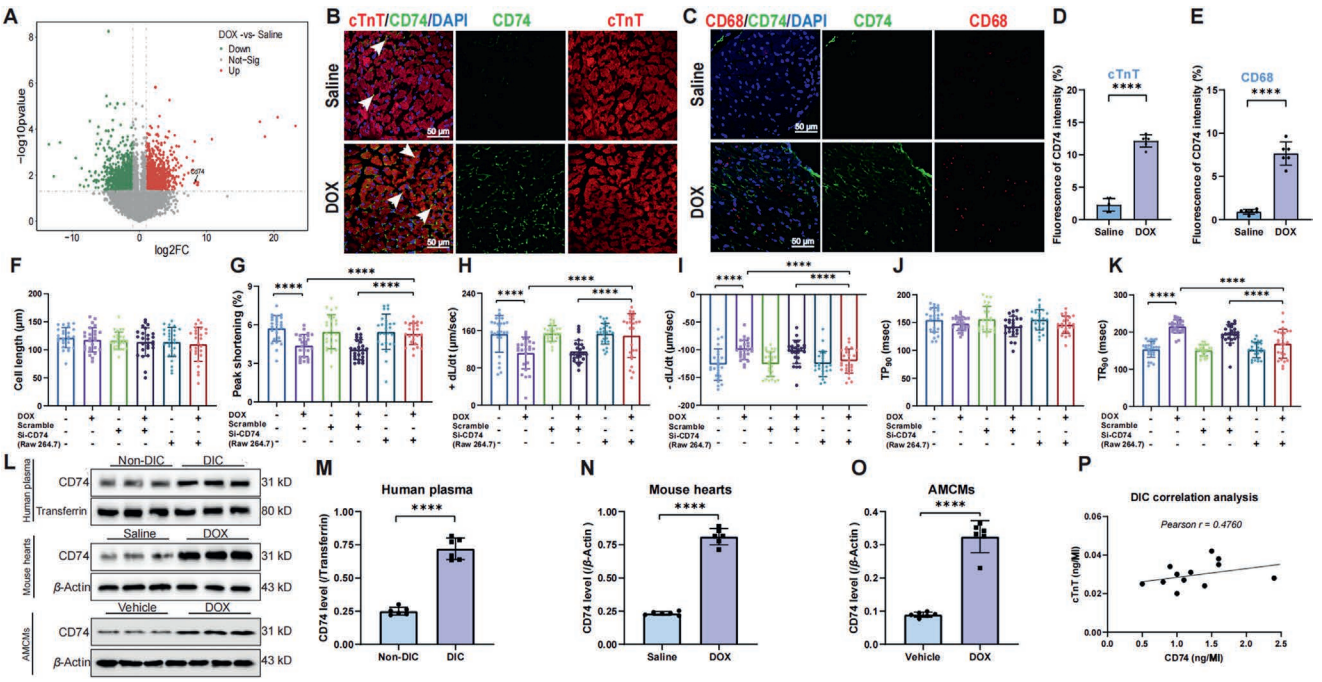

Figure 1 Change of CD74 levels in plasma from breast cancer patients with or without DOX exposure, myocardial tissues from mice subject to DOX-induced cardiomyopathy (DOX, 5 mg/kg, i.p. once per week for 4 weeks), and adult mouse cardiomyocytes exposed to DOX (1 μmol/L or 24 h). (A) Volcano plot of CD74 expression in mouse hearts with or without DOX exposure using GSE224157 dataset. (B, C) Immunofluorescence staining of CD74 (green) co-localized with cTnT (red) and CD68 (red) in mouse heart tissues with or without DOX exposure. (D, E) Fluorescence intensity of CD74. (F−K) In the RAW 264.7 macrophage and AMCM cell co-culture system, CD74 was knocked down in RAW 264.7 macrophages to discern its inhibitory effect on cardiomyocyte function with or without DOX exposure. Cell co-culture was performed using Transwell co-culture between RAW 264.7 macrophages and cardiomyocytes; (F) Resting cardiomyocyte cell length; (G) Cardiomyocyte peak shortening; (H) Cardiomyocyte maximal velocity of shortening (+dL/dt); (I) Maximal velocity of relengthening (−dL/dt); (J) Cardiomyocyte time-to-peak 90% shortening (TP_{90}); (K) Time-to-90% relengthening (TR_{90}). (L) Representative gel blots of CD74 in DIC from plasma of breast cancer patients, mouse hearts and adult mouse cardiomyocytes (AMCMs) with or without DOX exposure using specific antibodies (Transferrin or β-actin for loading control, transferrin for plasma protein). (M−O) Quantitative analysis of CD74 levels. (P) Association of CD74 with cTnT in plasma from DIC patients. Mean ± SEM; $n = 6$ images from 3 mice (panels B−E) per group, $n = 25$ cells (panels F−K), $n = 6$ (panel G) or 12 patients (panels J) and $n = 6$ mice (panels H and I) per group, $^*P < 0.05$ between indicated groups.

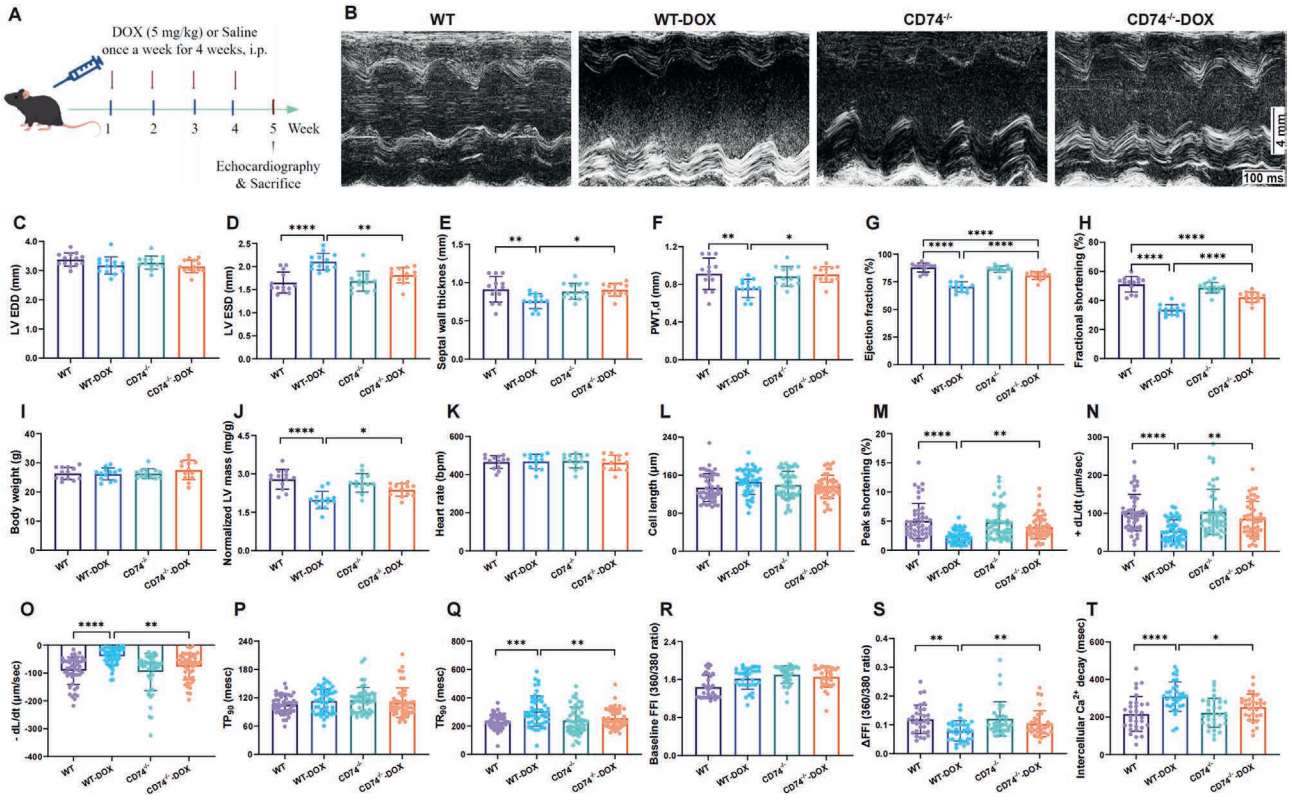

Figure 2 Echocardiographic, cardiomyocyte contractile and intracellular Ca^{2+} properties in 8-week-old WT and CD74$^{-/-}$ mice with or without DOX (5 mg/kg, i.p. once per week for 4 weeks) exposure. (A) Timeline of DOX treatments. (B) Representative echocardiographic images. (C) Left ventricular end-diastolic diameter (LV EDD). (D) Left ventricular end-systolic diameter (LV ESD). (E) Septal wall thickness. (F) Posterior wall thickness in diastole (PWT, d). (G) Ejection fraction. (H) Fractional shortening. (I) Body weight. (J) Normalized LV mass (to body weight). (K) Heart rate. (L) Resting cardiomyocyte cell length. (M) Cardiomyocyte peak shortening. (N) Cardiomyocyte maximal velocity of shortening ($+dL/dt$). (O) Maximal velocity of relengthening ($-dL/dt$); (P) Cardiomyocyte time-to-peak 90% shortening (TP_{90}). (Q) Time-to-90% relengthening (TR_{90}). (R) Baseline Fura-2 fluorescence intensity (FFI). (S) Electrically stimulated rise in FFI (ΔFFI) and (T) Intracellular Ca^{2+} decay rate. Mean ± SEM; $n = 13$ mice per group (panels B–J), $n = 48$ (panels L–Q) or 32 (panels R–T) per group from 3 to 5 mice, $^*P < 0.05$ between indicated groups.

SP8 confocal fluorescence microscope (Weztlar, Germany). For animal study, 2–3 images per heart were captured using a digital microscope (400 ×), with 5 mice per group analyzed.

2.10. *Cell culture, transfection and in vitro treatment*

Hearts from sterilized 8-week-old mice were enzymatically dispersed using collagenase type II (Cat No. 9001-12-1, Worthington), and cell lysates were purified through a Percoll gradient. RAW 264.7 macrophages, AMCMs and H9C2 cardiomyocytes were maintained in a Dulbecco's modified Eagle's medium (DMEM, Gibco), supplemented with 10% fetal bovine serum albumin (FBS, Gibco) under 5% CO_2 at 37 °C. The cell culture medium was refreshed every 24–48 h, and cells were passaged when they reached at least 70% confluence.

Plasmid or siRNA transfection was performed using Lipofectamine 3000 (Cat No. L3000008, Thermo Fisher) prior to biochemical evaluation 2–3 days later. The lentiviral vector encoding CD74 (hU6-MCS-CBh-gcGFP-IRES-puromycin) was obtained from GeneChem (Shanghai, China). In addition, a stable cell line mediated by this lentivirus was established. To prepare RAW 264.7 macrophage suspension, cell density was adjusted to 5×10^4 cells/mL using a complete medium. Cells were seeded into a culture plate and were incubated at 37 °C for 16–24 h until cells reached 20%–30% confluence. To perform viral infection, the required viral volume was calculated based on the MOI and virus titer using Eq. (1):

$$\text{Viral volume} = (\text{MOI} \times \text{Cell number})/\text{Viral titer} \quad (1)$$

The calculated viral volume was added to cells prior to 16-h incubation at 37 °C. Medium was replaced with fresh a complete medium and cells were cultured for 48–72 h post-infection. Then, puromycin (optimal concentration) was applied for 48 h to select infected cells. Complete death of uninfected controls was excluded. Puromycin concentration was then reduced to maintenance dose (1/2–1/4 selection concentration) for continued expansion. Cells were harvested for Western blot to validate infection efficiency.

2.11. *Transmission electron microscopy (TEM)*

TEM was used to evaluate mitochondrial ultrastructure. Heart tissues were fixed with glutaraldehyde, trimmed into small blocks, and cut into sections collected on 200-mesh copper grids for staining. Sections were visualized using an 80-kV transmission electron

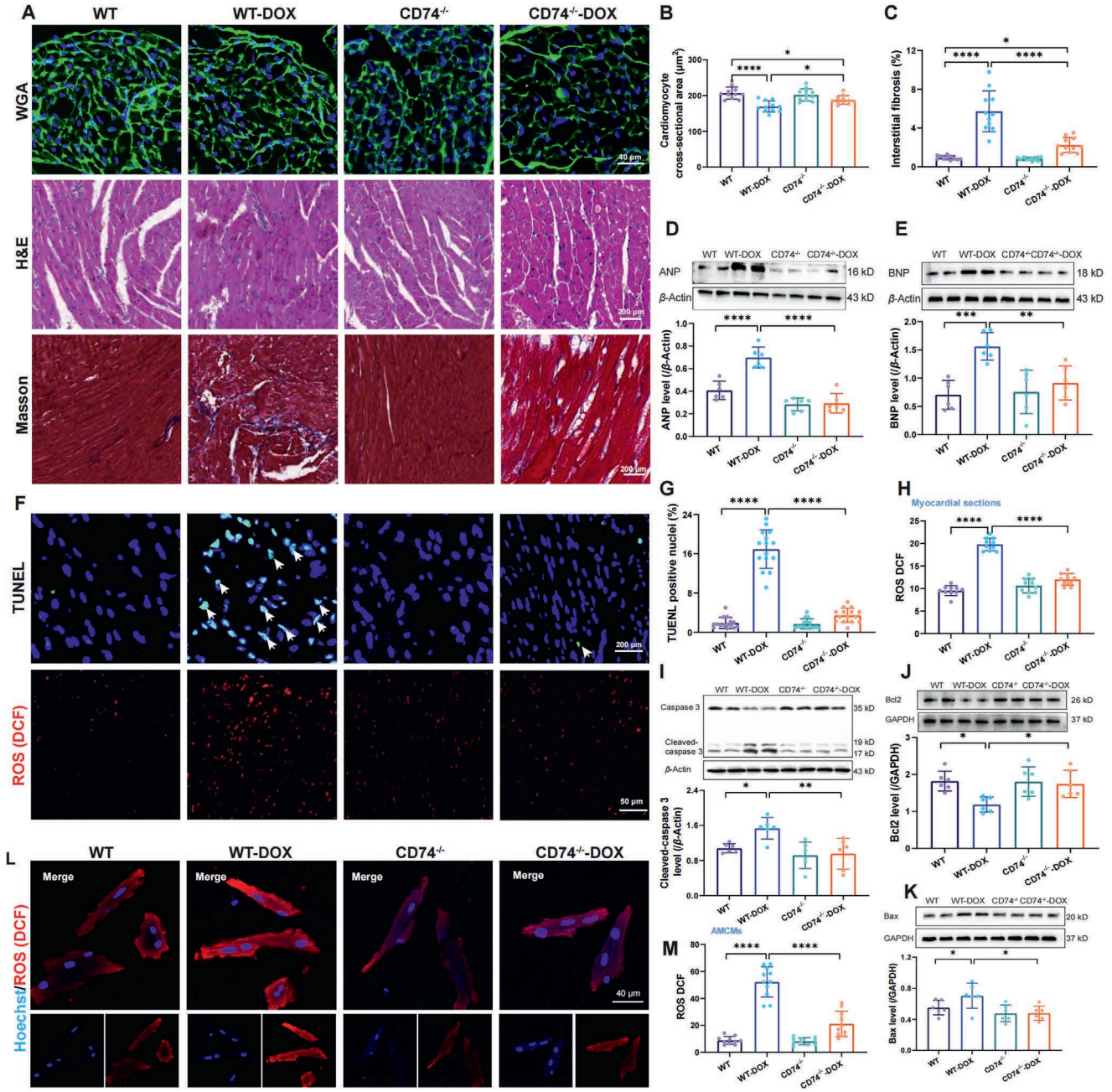

Figure 3 Wheat germ agglutinin (WGA), Hematoxylin and eosin (H&E), Masson trichrome, TUNEL, DCF staining, and protein markers for cardiac injury and apoptosis in 8-week-old WT and CD74$^{-/-}$ mice with or without DOX (5 mg/kg, i.p. once per week for 4 weeks) administration. (A) Representative WGA (upper row), H&E staining (middle row) and Masson staining (bottom row) from respective myocardial sections. (B) Quantitative analysis of cardiomyocyte cross-sectional area in WGA staining. (C) Quantitative analysis of interstitial fibrosis in MASSON staining. (D, E) Quantitative analysis of ANP and BNP level; Insets: Representative gel blots of ANP and BNP using specific antibodies (β-actin for loading control). (F) TUNEL (upper row) and DCF (lower row) staining of myocardial sections. (G) Quantitative analysis of TUNEL-positive cardiomyocytes. (H) Quantitative analysis of DCF staining; (I−K) Representative gel blots and quantitative analysis of Cleaved-caspase 3, Bcl2 and Bax. (L) Representative DCF of AMCMs from WT and CD74$^{-/-}$ mice with or without DOX exposure. (M) Pooled fluorescence intensity of DCF in AMCMs. Mean ± SEM; $n = 11$ images from 3 mice (panels A−C) per group, $n = 6$ mice (panels D, E, I−K) per group, $n = 10$−15 images from 3 to 5 mice (panels F−H, L, M), $^*P < 0.05$ between indicated groups.

microscope (JEM-1230; JOEL Ltd., Tokyo, Japan). At least 2 fields per slice at 8000 × magnification were observed, and 3 independent experiments were conducted for each group. The examiner was blinded during sample collection and data analysis. Mitochondrial size and axis lengths were measured using ImageJ software[38].

2.12. *Detection of mitochondrial membrane potential*

Mitochondrial membrane potential was measured using the JC-1 kit (Beyotime Institute of Biotechnology, Shanghai, China). In healthy mitochondria, JC-1 forms aggregate, emitting red

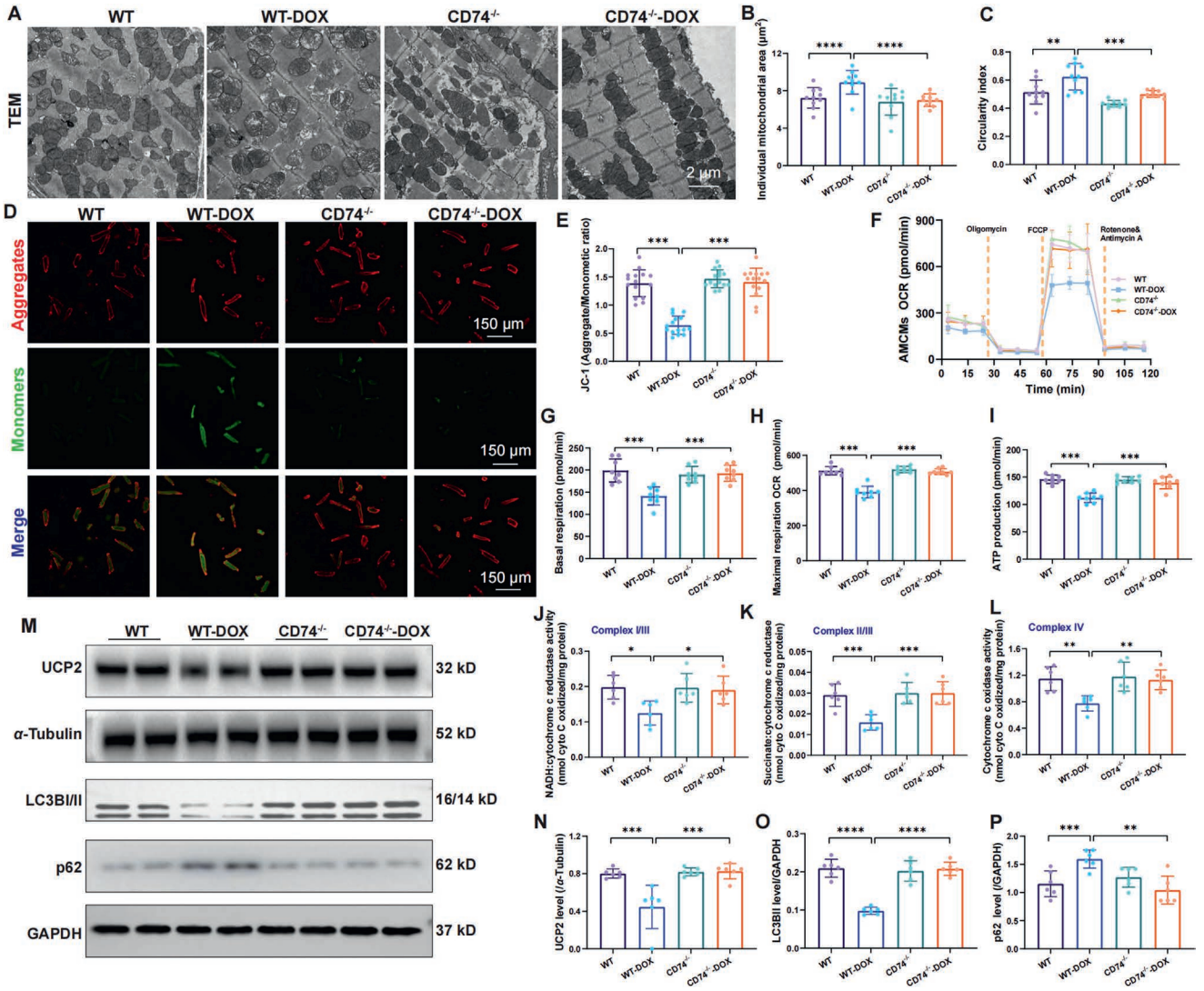

Figure 4 Mitochondrial ultrastructure and function, and Western blot analysis of autophagy in myocardium from 8-week-old WT and CD74$^{-/-}$ mice with or without DOX (5 mg/kg, i.p. once weekly for 4 weeks) insult. (A) Transmission electron microscopy (TEM) images showing mitochondria ultrastructure. (B) Individual mitochondrial area (μm^2). (C) Mitochondrial circularity (width-to-length ratio). (D) Representative JC-1 micrographs for aggregates (top row), monomer (middle row) and merged (bottom row) fluorescence. (E) Pooled JC-1 analysis. (F−I) OCR curves and quantification of basal respiration, maximal respiration, and ATP production in AMCMs from WT and CD74$^{-/-}$ mice with or without DOX challenge. (J−L) Mitochondrial respiration (complex I/III, complex II/III, and complex IV) in AMCMs from WT and CD74$^{-/-}$ mice with or without DOX challenge. (M) Representative gel blots of UCP2, LC3B and p62 using specific antibodies (α-Tubulin or GAPDH as loading control). (N−P) Quantitative analysis of UCP2, LC3B and p62 levels. Mean ± SEM; $n = 10$ visual fields (panels B and C) or $n = 15$ images (panels D, E) from 5 to 6 mice, and $n = 8$ (panels F−I) per group or $n = 6$ (panels J−L) per group from 3 mice, and $n = 6$ mice per group (panels M−P), $^*P < 0.05$ between indicated groups.

fluorescence, whereas in depolarized mitochondria, JC-1 remains in monomeric form, emitting green fluorescence. AMCMs were incubated with a JC-1 solution for 20 min at 37 °C according to the manufacturer's instructions. The red-to-green fluorescence ratio was quantified using ImageJ software[39].

2.13. *Measurements of cell bioenergetics*

Oxygen consumption rate (OCR) and ATP production were measured using a Seahorse XF96 analyzer (Agilent, Santa Clara, CA, USA). AMCMs were seeded into XFe96 plates at an appropriate density. OCR was measured using the Seahorse XF Cell Mitochondrial Stress Test (103015-100; Agilent). After baseline OCR recording, oligomycin, trifluoromethoxy carbonyl cyanide phenylhydrazone (FCCP), and rotenone/antimycin A were sequentially added to evaluate ATP-coupled respiration and maximal respiration[33].

2.14. *Mitochondrial electron transport chain enzymatic activity*

Cytochrome *c* oxidase (CCO) activity was assessed by measuring the absorbance change at 550 nm (ΔA_{550}), reflecting cytochrome *c* oxidation. The reaction was terminated by adding 0.17 mmol/L potassium cyanide when ΔA_{550} reached approximately 0.6 U. For

succinate: cytochrome *c* reductase activity, 12.5 mmol/L succinate was added and ΔA_{550} was recorded again. The reaction was halted using 17 mmol/L malonate. Finally, 2.8 nmol/L NADH was added to evaluate NADH: cytochrome *c* reductase activity by monitoring ΔA_{550}. Cytochrome *c* oxidation or reduction rates (nmol/min) were calculated using a molar extinction coefficient of 19,600[40].

2.15. Cell shortening/relengthening

Mechanical properties of adult mouse cardiomyocytes were assessed using an IonOptix soft-edge system (IonOptix, Milton, MA, USA). Cardiomyocytes were field stimulated at 0.5 Hz. Cell shortening and relengthening were assessed including cell length, peak shortening (PS, %), time-to-90% shortening (TP_{90}), time-to-90% relengthening (TR_{90}) and maximal velocity of shortening/relengthening ($\pm dL/dt$)[33].

2.16. Measurement of intracellular calcium

To measure intracellular calcium, cardiomyocytes were loaded with Fura-2/AM (0.5 μmol/L) for 15 min, and fluorescence intensity was recorded using a dual-excitation photomultiplier system (Ionoptix). Fluorescence emissions were detected between 480 and 520 nm, and changes in Fura-2 fluorescence intensity were inferred from the ratio at 360/380 nm. Single-exponential fluorescence decay was calculated as an indicator of intracellular Ca^{2+} clearance. Cells were field stimulated at 0.5 Hz. Fura-2-loaded cardiomyocytes were imaged using a confocal microscopy[41].

2.17. Iron measurement

AMCMs staining was performed to evaluate iron accumulation using the fluorescent probe FerroOrange (1 μmol/L, 20 min, Cat No. F374, Dojindo) for live-cell imaging of intracellular Fe^{2+}. Immunofluorescence was analyzed using a Leica SP8 laser confocal microscope (Germany) with a × 630 objective, employing excitation at 543 nm and emission at 580 nm[9].

2.18. Structure-based protein interaction interface analysis between CD74 and RRM2

The protein structures of CD74 and RRM2 were predicted using a template-based homology structure modeling tool SWISS-MODEL (www.swissmodel.expasy.org), Prediction results were visualized by the PyMol tool. CD74 using SWISS-MODEL temple structure P04233.1.A, chain A (covering residues 1−296, sequence identity 100.00%); RRM2 using SWISS-MODEL temple structure A0A7J8E4D4.1.A, chain A (covering residues 1−389, sequence identity 100.00%); Then, the protein−protein interaction was docked and modeled using the PRISM 2.0 server (http://cosbi.ku.edu.tr/prism) to predict their potential interaction interface.

2.19. Immunofluorescence and confocal imaging assay

Immunofluorescence for CD74 and RRM2 was performed per the manufacturer's instruction. Briefly, AMCMs and H9C2 cells were fixed and permeabilized at room temperature. Following a 1-h blocking, samples were incubated with the rabbit anti-CD74 (1:100) and the mouse anti-RRM2 (1:50) antibodies overnight at 4 °C. H9C2 cells were incubated with the anti-rabbit Alexa Fluor 488 (1:100) and anti-mouse Alexa Fluor 546 (1:800) secondary antibodies for 1 h in the dark. Immunofluorescence was assessed on a laser confocal microscope equipped with a × 630 oil objective (Leica sp8, Weztlar, Germany)[42].

2.20. Co-immunoprecipitation

The co-immunoprecipitation (Co-IP) assay was performed using a TheromFisher Pierce®Co-IP kit follow manufacturer's instructions. One hundred μg of purified anti-CD74, anti-RRM2, or anti-flag antibodies were coupled with resin. One mg protein samples were exposed to the antibody-coupled resin for 2 h. Protein−antibody complexes were eluted in 50 μL elution buffer after mixing and washing. The eluted protein samples were subjected to immunoblotting with corresponding antibodies[43].

2.21. Assessment of lipid peroxidation

Lipid peroxidation was assessed by BODIPY™ 581/591 C11 (Cat No. D3861, Thermo Fisher). Following drug treatment, AMCM cells were exposed to 5 μmol/L BODIPY for 30 min. Then, AMCM cells were visualized through a Leica sp8 confocal microscope (Wetzlar, Germany) at excitation wavelength of 581 nm and emission wavelength of 591 nm[44].

2.22. Molecular docking of CD74

The structure of CD74 protein (Uniprot: P04233) was obtained from the PDB database. The water molecules and heteroatoms were removed. The sdf file of Amifostine molecule (CAS Registry Number: 20537-88-6) required for docking was obtained from the Pubchem database and converted into mol2 structure. After hydrogenation and charge pretreatment of small molecules and proteins, AutoDockTool-1.5.6 was applied for molecular docking. Semi-flexible docking and Lamarck Genetic Algorithm were used, and the number of dockings was set to 50. Gridbox coordinates and size were set based on the information of protein active pockets, generated from POCASA1.1 website (http://altair.sci.hokudai.ac.jp/g6/service/pocasa/). Other parameters were set to the default values. Finally, results of molecular docking were visualized through PyMOL V4.6.0[33]. The top five molecular docking results are presented in Supporting Information Table S1.

2.23. Binding surface plasmon resonance (SPR) assay

For a deeper investigation on the interaction between CD74 and DOX, SPR-based binding analysis was performed[45]. All real-time biomolecular interactions were analyzed using a BIAcore T200 system (GE Healthcare) in HBS-EP buffer (10 mmol/L HEPES-NaOH, pH 7.4, 500 mmol/L NaCl, 3 mmol/L EDTA, 0.1% Surfactant P20) at 25 °C. To determine the binding affinity of doxorubicin hydrochloride to CD74, CD74 protein was immobilized onto the flow channels of a CM5 sensor chip (GE Healthcare) *via* amine coupling, while a control flow channel was left blank. A dilution series of doxorubicin hydrochloride (10, 5, 2.5, 1.25, 0.625, 0.3125 μg/mL) was prepared in HBS-EP buffer and injected over the CD74 chip at a flow rate of 10 μL/min for 60 s. Following each injection, HBS-EP buffer was flowed over the chip at the same rate to monitor dissociation. The sensor chip was regenerated by injecting 50 mmol/L NaOH and 1 mol/L NaCl at 10 μL/min for 30 s. Data were processed using BIA-Evaluation software; equilibrium dissociation constants (K_D) were calculated from fitted saturation binding curves.

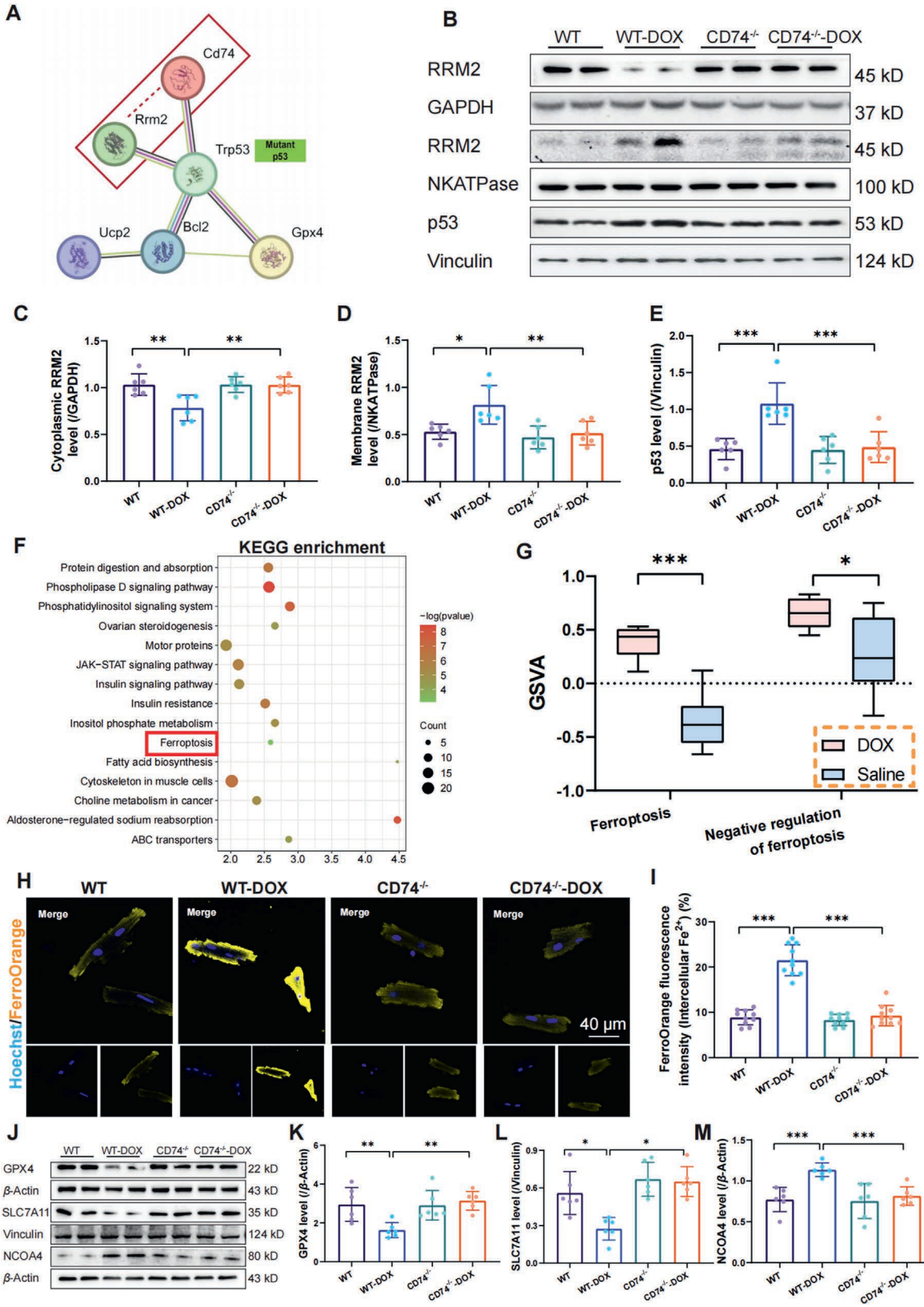

Figure 5 CD74/RRM2 interaction, its impact on CD74/RRM2 distribution and ferroptosis in 8-week-old WT and CD74$^{-/-}$ mice with or without DOX (5 mg/kg, i.p. once per week for 4 weeks) exposure. (A) The protein−protein interaction network was conducted using the STRING database. (B) Representative gel blots depicting RRM2 and p53 levels (GAPDH or NKATPase as loading control, NKATPase for cell membrane protein). (C, D) Quantitative analysis of RRM2 in cytoplasm and cell membrane. (E) Quantitative analysis of p53 level. (F) KEGG enrichment

2.24. Quantitative detection of lipid peroxides

Following homogenization and lysis of tissues or cells, the supernatant was collected for quantification of malondialdehyde (MDA) quantification, a key lipid peroxidation marker. Standards and working solutions were prepared according to the manufacturer's instructions. The standard and test samples (1 μL) were transferred to centrifuge tubes, followed by the addition of 0.2 mL of MDA working solution. The mixtures were vortexed and then incubated at 100 °C for 15 min. After cooling to room temperature, samples were centrifuged at $1000\times g$ for 10 min, and 200 μL of the supernatant was transferred onto a 96-well plate. A blank control was included, and the absorbance was measured at 532 nm. MDA content was calculated[46].

2.25. Enzyme-linked immunosorbent assay (ELISA)

According to the manufacturer's protocol, levels of inflammatory factors in mouse serum were detected using the mouse interleukin-6 (IL-6) enzyme-linked immunosorbent assay (ELISA) kit (ab222503, Abcam) the tumor necrosis factor-α (TNF-α) (ab208348, Abcam), and interleukin 1β (IL-1β) (Cat#: 1210122, Dakewe) ELISA Kit[47].

2.26. Western blot analysis

Heart tissues were sonicated in a lysis buffer containing 20 mmol/L Tris (pH 7.4), 150 mmol/L NaCl, 1 mmol/L EDTA, 1 mmol/L EGTA, 1% Triton, 0.1% sodium dodecylsulfate, and a protease inhibitor cocktail. Protein samples were incubated with anti-CD74, anti-caspase3, anti-Bax, anti-Bcl2, anti-UCP2, anti-LC3B, anti-p62, anti-RRM2, anti-p53, anti-GPX4, anti-SLC7A11, anti-NCOA4, anti-ANP, anti-BNP (1:1000 dilution), Horseradish peroxidase-coupled secondary antibodies were employed. All antibodies were obtained from Cell Signaling Technology (Danvers, MA, USA), or Abcam (Shanghai, China). After immunoblotting, films were scanned and detected using a Bio-Rad calibrated densitometer (GS-900, Shanghai, China) and band intensity was normalized to loading controls transferrin, α-tubulin, β-actin, Vinculin, GAPDH or NKATPase. All antibodies employed for Western blot or immunofluorescence are included in Supporting Information Table S2. To avoid overlapping of protein bands during electrophoresis and subsequent immunoblotting, an internal reference protein with distinct and appropriate molecular weight, as well as stable expression, was selected based on the sample type and the molecular weight of the target protein.

2.27. Statistical analysis

Data are presented as mean ± standard error of the mean (SEM). Independent samples *t*-test or Wilcoxon rank sum test for continuous variables were employed when appropriate to examine differences between DIC and non-DIC human subjects. Statistical significance was estimated using one-way analysis of variance (ANOVA) followed by Tukey's multiple comparison test, repeated measures ANOVA in R and Bonferroni adjusted test. The CD74 and cTnT contents were analyzed for correlation using Pearson's coefficient. $^*P < 0.05$ were indicated for significance. All statistics analyses were performed using GraphPad Prism 9.0 software (GraphPad, San Diego, CA, USA).

3. Results

3.1. Single cell RNA sequencing analysis of tumor bearing mice administered DOX and plasma CD74 levels in patients of DIC

Single cell RNA sequencing (scRNA-Seq) was performed in tumor derived cells from each DOX responsive domain (Saline, DOX-resistant and DOX-sensitive). The corresponding cell annotation results are shown in Supporting Information Fig. S1A. The percentage of T cells was decreased in drug-resistant tumors (2.96%) and sensitive tumors (1.84%) compared to saline-treated controls (16.39%) (Fig. S1B). Further analysis indicates that the $CD4^+$ T cells were significantly decreased with regards to the composition of T cell subsets. The proportion of $CD4^+$ T cells was 7.1% and 15.5% in resistant tumors and sensitive tumors, respectively, while proportion of $CD8^+$ T cells was 84.8% and 67.6% in resistant tumors and sensitive tumors, respectively (Fig. S1C). This phenomenon is contrary to the situation of DOX-induced cardiac injury. In DIC, other than oxidative stress, DNA damage and mitochondrial injury, immune inflammatory response represents another essential pathological machinery[48]. From the results obtained on the STRING website, the receptors of $CD4^+$ T cells include CD74, H2-Eb1, H2-Eb2 and others (Fig. S1D). Functional enrichment analysis of gene ontology (GO) showed that DEGs were overtly enriched within "T cell differentiation" (Fig. S1E). In addition, CD74 acts upstream of or within several processes, including antigen processing and presentation of exogenous peptide antigen *via* MHC class II, regulation of T cell differentiation and thymic T cell selection[49]. Next, we examined the differences in CD74 gene expression levels across five cell types within three sample groups (Fig. S1F). Surprisingly, we found no significant differences in CD74 gene expression among the three groups. Notably, the differential expression level of CD74 gene in macrophages and T cells caught our attention. Consequently, we conducted experiments to further examine the expression of CD74 in immune cells.

As reported in previous research, CD74 expression was found to be elevated in T cells of patients with severe COVID-19[50]. In our transcriptomic analysis of myocardial tissues from DIC mice (GSE224157), we similarly observed a significant increase in CD74 expression in the DIC group (Fig. 1A). To further investigate, we performed CD74 and cTnT, CD68 immunofluorescence staining on myocardial tissues from DIC mice. The results showed a marked increase in CD74 expressions in myocardial tissues, while no significant changes were observed in macrophages or T

from transcriptomics data of DIC mice (GSE224157). (G) Application of gene set variation analysis (GSVA) for calculation of the activity level of ferroptosis pathway from transcriptomics data of DIC mice (GSE224157). (H) Intracellular Fe^{2+} detected using the FerroOrange probe in AMCMs from WT and $CD74^{-/-}$ mice with or without DOX exposure. (I) Fluorescence intensity of intracellular Fe^{2+}. (J) Representative gel blots of GPX4, SCL7A11 and NCOA4 (β-Actin or Vinculin as loading control). (K−M) Quantitative analysis of GPX4, SCL7A11 and NCOA4 levels. Mean ± SEM; $n = 6$ mice (panels B−E, J−M) or $n = 10$ fields from 3 mice (panels H, I) per group, $^*P < 0.05$ between indicated groups.

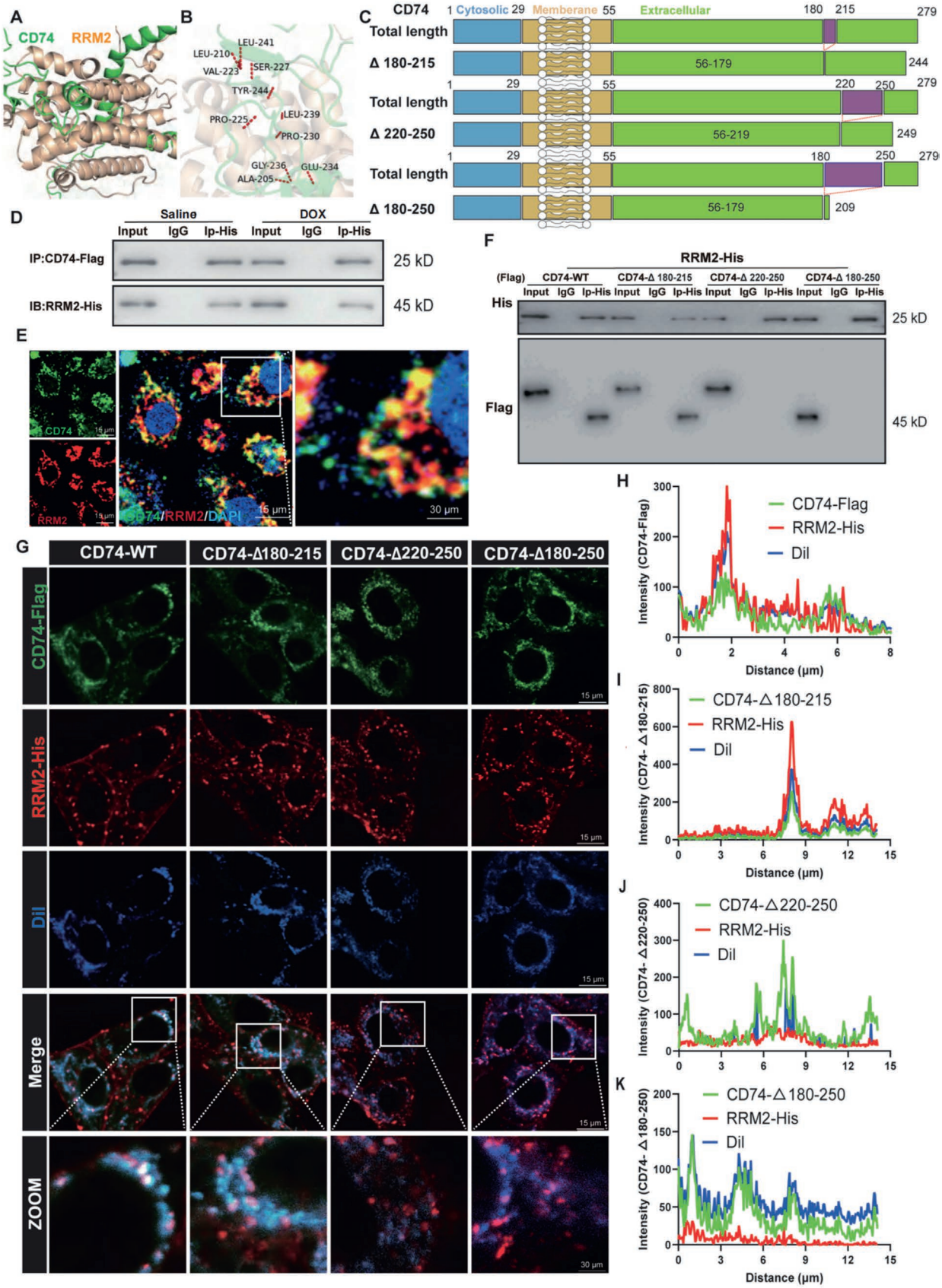
A
CD74
RRM2
B
LEU-241
LEU-210
SER-227
VAL-223
TYR-244
PRO-225
LEU-239
PRO-230
GLY-236
GLU-234
ALA-205
C
CD74
1 Cytosolic 29 Memberane 55 Extracellular 180 215 279
Total length
Δ 180-215
56-179
244
Total length
Δ 220-250
56-219
249
Total length
Δ 180-250
56-179
209
D
Saline
DOX
Input IgG Ip-His Input IgG Ip-His
IP:CD74-Flag
IB:RRM2-His
25 kD
45 kD
E
CD74
RRM2
CD74/RRM2/DAPI
15 μm
30 μm
F
RRM2-His
(Flag) CD74-WT CD74-Δ 180-215 CD74-Δ 220-250 CD74-Δ 180-250
Input IgG Ip-His Input IgG Ip-His Input IgG Ip-His Input IgG Ip-His
His
Flag
25 kD
45 kD
G
CD74-WT
CD74-Δ180-215
CD74-Δ220-250
CD74-Δ180-250
CD74-Flag
RRM2-His
Dil
Merge
ZOOM
15 μm
30 μm
H
CD74-Flag
RRM2-His
Dil
Intensity (CD74-Flag)
Distance (μm)
I
CD74-Δ180-215
RRM2-His
Dil
Intensity (CD74- Δ180-215)
Distance (μm)
J
CD74-Δ220-250
RRM2-His
Dil
Intensity (CD74- Δ220-250)
Distance (μm)
K
CD74-Δ180-250
RRM2-His
Dil
Intensity (CD74- Δ180-250)
Distance (μm)

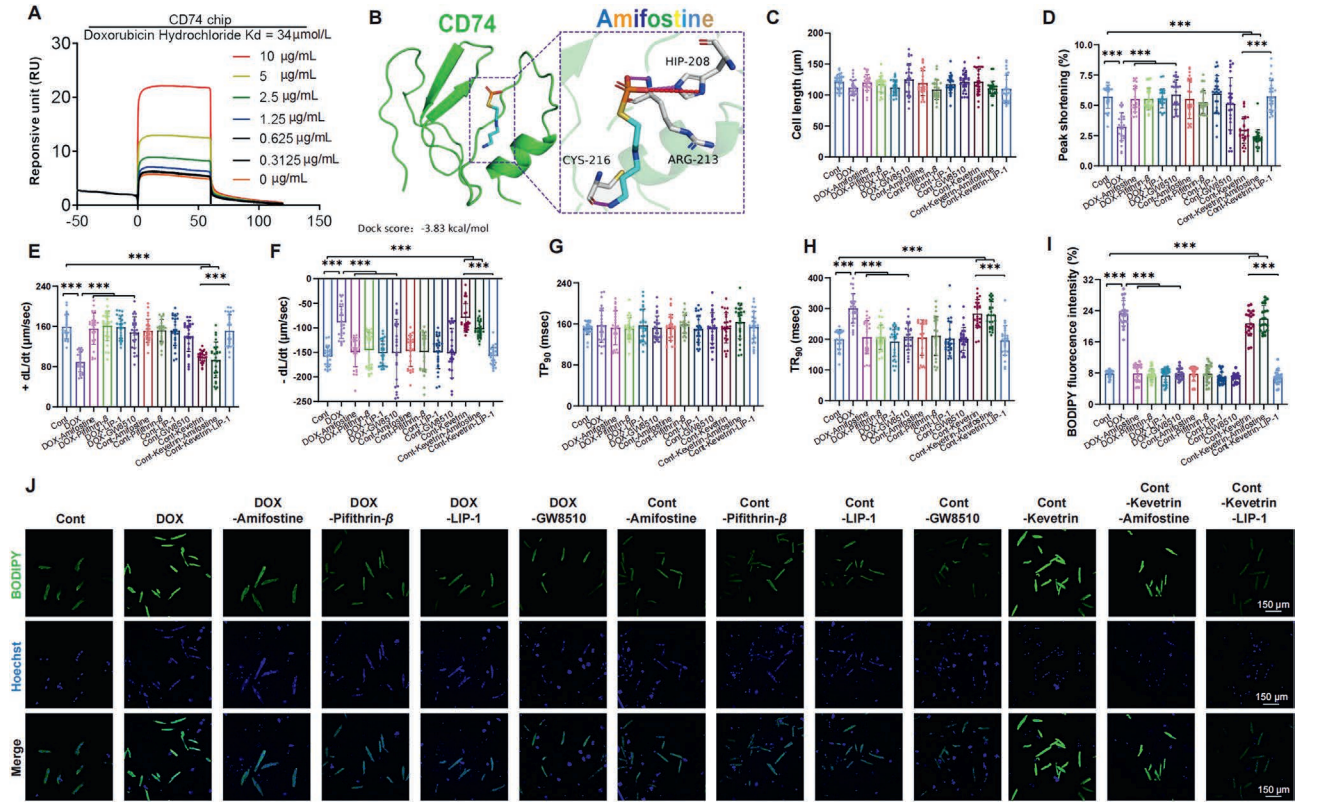

Figure 7 Protection of DOX-induced ferroptosis and cardiotoxicity with pharmacological inhibition of CD74. (A) Surface plasmon resonance (SPR) assay the binding of CD74 and DOX. (B) Molecular docking simulation of the binding between Amifostine and CD74. (C−I) AMCMs were exposed to DOX (1 μmol/L) for 24 h, prior to an additional 24-h treatment with or without Amifostine (10 μmol/L), Pifithrin-β (10 μmol/L), Kevetrin (80 μmol/L), LIP-1 (200 nmol/L), or GW8510 (4 μmol/L). (C) Cell length. (D) Peak shortening. (E) Maximal velocity of shortening (+dL/dt). (F) Maximal velocity of relengthening (− dL/dt). (G) Time-to-peak 90% shortening (TP_{90}). (H) Time-to-90% relengthening (TR_{90}). (I) Quantified BODIPY fluorescence intensity. (J) Representative BODIPY staining images from respective cell groups. Mean ± SEM; $n = 26$ (panels C−H) or 20 (panels I, J) per group from 3 mice, $^*P < 0.05$ between indicated groups.

cells. This suggests that CD74 is primarily localized in cardiomyocytes and plays a role in DIC, without co-localization in macrophages and T cells (Fig. 1B−E, Fig. S1G and S1H). These findings further confirm that CD74 does not exert its function in DIC by activating T cells or macrophages, but rather through cardiomyocytes.

Subsequently, a co-culture study was performed between Raw 264.7 macrophages and cardiomyocytes, in which CD74 was knocked down specifically in Raw 264.7 macrophages. A Transwell co-culture system was employed to investigate whether the role of CD74 in DOX-induced myocardial injury was dependent upon macrophages. In a DOX-induced primary cardiomyocyte injury model, we first assessed knockdown efficiency of CD74 and quantified expression of inflammation-related cytokines, including IL-6, IL-1β, and TNF-α. As expected, DOX exposure overtly increased levels of inflammatory markers in the culture medium. Notably, CD74 knockdown (not scramble RNA) in macrophages markedly attenuated levels of IL-6, IL-1β, and TNF-α in culture medium (Fig. S1I−S1L). Furthermore, the Transwell co-culture of cardiomyocytes with CD74-deficient macrophages significantly improved contractile function of AMCMs in the face of DOX challenge (Fig. 1F−K). Finally, blood samples from DIC patients were analyzed, revealing elevated plasma CD74 levels, consistent with increased CD74 expression in mouse heart tissue and AMCMs cell under DIC conditions (Fig. 1L−O). Notably, plasma CD74 levels showed a positive correlation with cTnT in DIC

Figure 6 Interaction of CD74 with RRM2 through 180−215 amino acid domain for recruitment of RRM2 onto cytomembrane. (A, B) Structure-based interface analysis between CD74 and RRM2. CD74−RRM2 complex structure with interaction hot-spot residues labeled using PRISM. (C) Graph illustrating construction of CD74 (total length) and mutants (Delta 180−215 aa, Delta 220−250 aa, Delta 180−250 aa). (D) IP analysis of CD74 tagged with Flag (CD74-Flag) and RRM2 tagged with His (RRM2-His) from AMCMs from WT and $CD74^{-/-}$ mice with or without DOX exposure (5 mg/kg, i.p. once per week for 4 weeks). (E) Representative fluorescent images for co-localization of CD74 (green) with RRM2 (red) using H9C2 cells. (F, G) IP analysis of CD74 tagged with Flag (CD74-Flag) and RRM2 tagged with His (RRM2-His); H9C2 cells were divided into 4 groups (CD74-Flag, Delta 180−215 aa, Delta 220−250 aa, Delta 180−250 aa) prior to transfection of RRM2 using plasmid DNA, Confocal image exhibiting H9C2 cells transfected with indicated plasmids, stained with Dil (blue), anti-CD74 (green), and anti-RRM2 (red) antibodies. (H−K) Fluorescence intensity curve of CD74 and RRM2 in co-localization images.

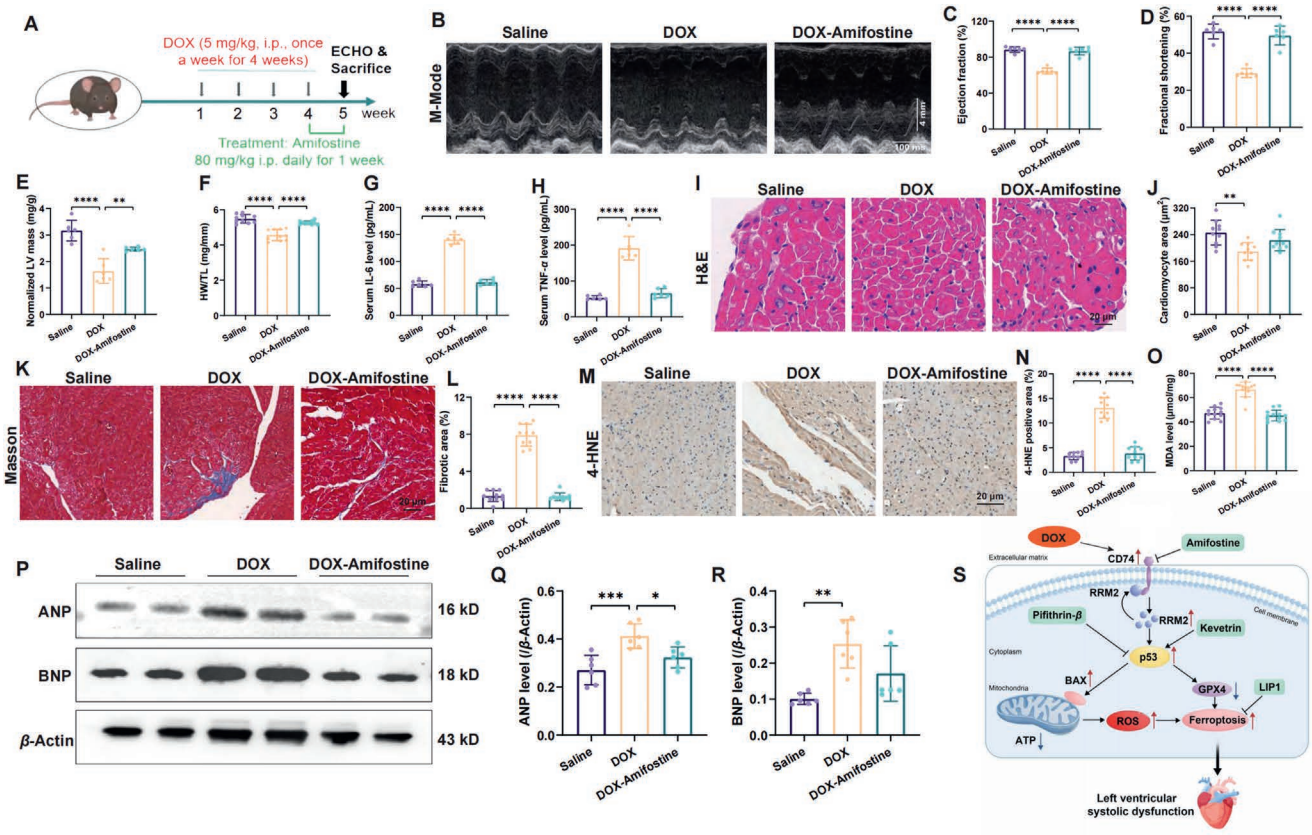

Figure 8 Protection of DOX-induced ferroptosis and cardiotoxicity with pharmacological inhibition of CD74. (A) Timeline of DOX and Amifostine treatments; DOX was administered to C57BL/6J mice for a period of 4 weeks. Beginning in the fifth week, Amifostine (80 mg/kg, once daily) was administered for an additional week. (B) Representative M-mode echocardiographic images. (C−F) Pooled analysis of left ventricular ejection fraction, fractional shortening, normalized LV mass, and heart weight normalized to tibial length (HW/TL). (G, H) Serum IL-6 and TNF-α levels. (I) Representative H&E staining micrographs from respective groups. (J) Quantitative analysis of cardiomyocyte area. (K) Representative Masson trichrome staining images. (L) Quantitative analysis of interstitial fibrosis. (M, N) 4-HNE staining images and 4-HNE positive area. (O) Malondialdehyde (MDA) levels in heart tissues. (P−R) Representative gel blots and quantitative analysis of ANP, BNP using specific antibodies (β-Actin as loading control); and (S) Schematic diagram illustrating summarized experimental findings and cell signaling pathways involved in CD74 ablation-evoked benefit against DIC. Mean ± SEM; $n = 6$ mice (panels B−H, P−R) or $n = 10$ per group from 3 mice (panels I−N) or $n = 12$ from 3 mice (panel O) per group, $^*P < 0.05$ between indicated groups.

patients (Fig. 1P), further supporting its potential role in DIC pathophysiology.

3.2. *Effect of CD74 on DOX-induced changes in myocardial function, morphology, mechanical properties, and intracellular Ca^{2+} responses*

Our findings demonstrate that DOX induced significant alterations in cardiac remodeling, marked by alterations in left ventricular end-systolic diameter (LVESD), septal wall thickness, diastolic posterior wall thickness (PWT, d), and normalized left ventricular mass, all of which were mitigated by CD74 ablation. Additionally, CD74 knockout partially restored ejection fraction and fractional shortening, while CD74 deletion alone had no intrinsic effects. Cardiomyocyte mechanical assessment revealed that DOX exposure significantly suppressed peak shortening, maximal velocity of shortening/relengthening ($\pm dL/dt$) and prolonged relengthening duration (TR_{90}) without affecting resting cell length and time-to-90% shortening (TP_{90}), the effect of which was reversed by CD74 knockout without any effect from CD74 deletion itself. To elucidate the mechanisms underlying CD74 ablation-elicited protection, intracellular Ca^{2+} handling was assessed using Fura-2 imaging. DOX suppressed electrically stimulated rise in intracellular Ca^{2+} (ΔFFI) and prolonged intracellular Ca^{2+} decay without affecting resting intracellular Ca^{2+} levels, the effect of which was nullified by CD74 ablation without any effect from CD74 knockout itself (Fig. 2).

3.3. *Effect of CD74 on DOX-induced changes in myocardial fibrosis, oxidative stress and apoptosis*

Our results revealed that CD74 knockout rescued DOX-induced interstitial fibrosis, oxidative stress and apoptosis. WGA and Masson staining displayed DOX-induced cardiomyocyte atrophy and myocardial interstitial fibrosis, which were partially attenuated by CD74 knockout (Fig. 3A−C). Along the same line, DIC upregulated genes including ANP, and BNP as well as apoptosis markers including cleaved-caspase 3, Bax and Bcl2, the effects were reversed by CD74 knockout (Fig. 3D−E, I−J, K). Consistently, CD74 deficiency nullified DOX-induced TUNEL apoptosis and oxidative stress (DCF staining of heart tissue and AMCMs) without any effect from CD74 ablation itself (Fig. 3F−H, L−M).

In DIC mice, the efficiency of CD74 knockout was verified (Supporting Information Fig. S2A).

3.4. Effect of CD74 ablation on DIC ultrastructural, mitochondrial changes and changes in apoptosis and autophagy

Myocardial ultrastructure and mitochondrial membrane potential were evaluated using TEM and JC-1 staining respectively. DOX exposure elicited overt cytoarchitectural aberrations, including mitochondrial swelling (increased mitochondrial circular index and individual mitochondrial area), cristae fracture, sarcomere distortion, and disruption of myocardial filaments. However, the effects of which were alleviated by CD74 knockout. CD74 knockout alone did not exert any notable change on mitochondrial ultrastructure (Fig. 4A−C). This is supported by changes in MMP where DIC collapsed MMP (aggregate-to-monomer ratio), the effect of which was obliterated by CD74 knockout without notable effect from CD74 ablation itself (Fig. 4D and E). Mitochondrial stress tests revealed that DOX-challenged cardiomyocytes exhibited significantly reduced basal respiration, maximal respiration, and ATP-coupled respiration, along with impaired respiration through complexes I/III, II/III and IV. These effects were rescued by CD74 knockout (Fig. 4F−L), suggesting a role for CD74 in mitochondrial regulation. Measurement of mitochondrial protein UCP-2 offered further support on CD74 ablation-induced protection against DOX-induced mitochondrial injury. Our data also revealed the upregulated autophagy adaptor p62 along with suppressed LC3BII in DIC hearts, the effect of which was attenuated by CD74 knockout with little response from CD74 ablation itself (Fig. 4M−P). These results suggest that CD74 confers cardioprotection against DIC by mitigating DOX-induced mitochondrial and autophagic dysfunction. Specifically, DOX impairs autophagy, and CD74 knockout alleviates this blockade, further highlighting CD74's role in maintaining mitochondrial homeostasis and cardiomyocyte survival.

3.5. Change in CD74 and iron levels in DIC, influence of CD74 ablation on RRM2/p53 in ferroptosis

With a perceived role in several biological processes, including macrophage migration inhibitory factor (MIF) signaling regulation, ribonucleotide reductase (RR) plays a crucial role in DNA synthesis to limit its repair[51]. CD74 and CXCR2 are the currently known receptors for MIF, although the specific mechanism underlying receptor regulation remains elusive[52]. Earlier evidence has revealed a vital role for RRM2 in promoting cell proliferation, migration, and invasion, alongside with inhibition of cell apoptosis[53]. Moreover, RRM2 appears to regulate DOX-induced cardiotoxicity through an AKT/mTOR-dependent manner[54]. In this context, protein markers of CD74, RRM2, p53 and ferroptosis were evaluated to discern possible cell signaling mechanisms in DIC and CD74 knockout-induced changes in cardiac remodeling and function. Findings from the protein−protein interaction network using STRING software indicated that CD74, RRM2, p53, Bax, UCP2 and GPX4 were cross-connected (Fig. 5A). Under DIC conditions, myocardial RRM2 levels in the cytoplasm were overtly reduced, an effect reversed by CD74 knockout. Conversely, RRM2 expression on the cell membrane was significantly increased following DOX exposure, which was reconciled by CD74 knockout. Given that p53 (*TP53* gene) is a key regulator in breast cancer and DOX-related toxicity[55,56], we evaluated levels of p53 and found that DOX exposure overtly upregulated p53, an effect reverted by CD74 knockout (Fig. 5B−E). Volcano plot analysis further demonstrated that GPX4 and SLC7A11 were downregulated, while TP53 and NCOA4 were significantly upregulated in the context of ferroptosis. KEGG enrichment analysis identified differentially expressed proteins related to ferroptosis and apoptosis in DOX-treated cancer cells (GSE244574). Similarly, GSVA6 analysis of scRNA-Seq (GSE 205551) indicated active ferroptosis and its negative regulation in DOX-sensitive cells (Supporting Information Fig. S3A−S3C). Transcriptomic data from the DOX-induced mouse DIC model also revealed enrichment of ferroptosis pathways in KEGG and GSVA (Fig. 5F and G), reinforcing the role of ferroptosis in tumorigenesis and myocardial injury. Fluorescence intensity analysis confirmed a significant increase in intracellular Fe^{2+} levels in the DOX group, which was attenuated by CD74 knockout (Fig. 5H and I). We next examined the possible involvement of CD74 in the regulation of ferroptosis and found that DOX exposure overtly downregulated GPX4 and SLC7A11, two vital biomarkers for ferroptosis, while upregulating NCOA4-mediated ferritinophagy. These effects were mitigated by CD74 knockout, whereas CD74 knockout alone had little impact (Fig. 5J−M).

3.6. Interaction and distribution between CD74 and RRM2

The known cellular functions for CD74 include facilitating MHC class II protein expression (as the intracellular invariant chain) and mediating MIF signaling activity. To identify potential CD74-interacting proteins, we utilized the template-based homology structure modeling tool SWISS-MODEL. CD74 consists of three distinct domains including topologically intracellular (aa 1−29), transmembrane (aa 33−55), and an extracellular domain (aa 56−279). Further immunoprecipitation analysis revealed a strong interaction between CD74 and RRM2 in cardiomyocytes (Fig. 6A). Prism software predicted CD74 binding sites for RRM2, indicating that the interaction was localized within an unidentified domain, with the CD74 extracellular segment (aa 220−250) showing the highest binding probability (Fig. 6B). To validate this, CD74 mutants targeting these regions were constructed (Fig. 6C). The results shown in Fig. 6D and E confirmed a significant interaction between CD74 and RRM2. Further immunoprecipitation analysis revealed that the CD74 extracellular domain (aa 220−250) mediated the CD74/RRM2 interaction, whereas the CD74 segment (aa 180−215) did not participate in the bind with RRM2 (Fig. 6F). Given these findings, CD74 may interact with RRM2 in the cytomembrane or cytoplasm, potentially influencing its transport and distribution. To examine whether CD74 affects RRM2 localization in H9C2 cells, we assessed co-localization levels of CD74 and RRM2 in both the cytomembrane and cytoplasm (Fig. 6 G−K). The data indicate that CD74 promotes RRM2 translocation to the cytomembrane, suggesting a regulatory role of CD74 in RRM2 distribution within the cell.

3.7. Effect of CD74/RRM2 interaction ferroptosis and DOX-induced cardiomyocyte contractile dysfunction

Recombinant CD74 proteins were immobilized onto the chips, and the binding interaction between CD74 and DOX (0, 0.3125, 0.625, 1.25, 2.5, 5, and 10 μg/mL) was assessed using surface plasmon resonance (SPR). As shown in Fig. 7A, CD74 bound to DOX with a dissociation constant (K_D) of 34 μmol/L. To further investigate the binding properties, molecular docking analysis was

performed using AutoDock. The binding capacity and interaction mode of the top-ranked molecule Amifostine, with CD74 were evaluated based on the binding energy scores (Table S1). As illustrated in Fig. 7B, Amifostine formed traditional hydrogen bonds with HIP208, ARG213, and CYS216, with a docking and binding energy of −3.83 kcal/mol, indicating a strong interaction between Amifostine and CD74.

To elucidate the role of the CD74/RRM2/p53 cascade in DOX-induced myocardial responses and CD74 ablation, cardiomyocyte contractile function and ferroptosis were evaluated in adult murine cardiomyocytes (AMCMs) treated with DOX for 24 h in the absence or presence of the chemoprotective agent Amifostine (10 μmol/L)[26], the p53 inhibitor Pifithrin β (10 μmol/L)[35], the p53 activator Kevetrin (80 μmol/L), the ferroptosis inhibitor LIP-1 (200 nmol/L) and RRM2 inhibitor GW8510 (4 μmol/L) for an additional 24 h. Analysis of cardiomyocyte contractile property showed that DOX exposure suppressed peak shortening, maximal velocity of shortening/relengthening ($\pm$dL/dt), while prolonging time-to-90% relengthening (TR_{90}), without affecting resting cell length and time-to-90% shortening (TP_{90}). Amifostine attenuated DOX-induced cardiomyocyte mechanical abnormalities, the effect of which was abolished by p53 activator Kevetrin. Additionally, RRM2 inhibition ameliorated DOX-induced contractile dysfunction. Notably, Amifostine had no effect on cardiomyocyte mechanical indices in the absence of DOX exposure (Fig. 7C−H). Furthermore, Amifostine alleviated DOX-induced ferroptosis, as evidenced by a reduction in BODIPY fluorescence, indicating decreased lipid peroxidation (Fig. 7I and J). However, the anti-ferroptotic effect of Amifostine was negated by the p53 activator Kevetrin. Similarly, RRM2 inhibition mitigated lipid peroxide accumulation (Fig. 7I and J). These findings suggest that the anti-ferroptotic properties induced by CD74/RRM2 deficiency are p53-dependent.

3.8. Pharmacological inhibition of CD74 by Amifostine prevents DIC and cardiomyocyte ferroptosis

Amifostine (WR-2721) is a cytoprotective agent initially developed as a radioprotectant, shielding normal tissues from radiation and cytotoxic agents while having a lesser effect on tumors, expanding the therapeutic window. Preclinical and clinical studies show it reduces chemotherapy-induced hematological toxicity, neurotoxicity, nephrotoxicity, and ototoxicity when administered before treatment[57,58]. To assess the pathophysiological impact of Amifostine in DIC, we evaluated its pharmacological inhibition in a murine model. C57BL/6J mice received DOX for 4 weeks, followed by Amifostine (80 mg/kg, once daily) in the fifth week (Fig. 8A). Amifostine significantly alleviated DOX-evoked unfavorable changes in LV mass (normalized), ejection fraction, fractional shortening, and heart weight (HW)-to-tibial length ratio (Fig. 8B−F). It also attenuated DOX-induced elevation of serum inflammatory markers IL-6 and TNF-α, cardiomyocyte atrophy and interstitial fibrosis (Fig. 8G−L), while reducing lipid peroxidation (4-HNE and MDA), and cardiac injury biomarkers ANP and BNP (Fig. 8M−R). These findings highlight a protective role for Amifostine as a CD74 inhibitor in DOX-induced cardiotoxicity.

4. Discussion

The salient findings from our study revealed a favorable response for CD74 ablation against DOX-induced cardiotoxicity. DOX challenges overtly upregulated CD74 levels, in line with elevated soluble plasma CD74 levels in breast cancer patients exposed to DOX. Our results revealed that DOX evoked cardiac remodeling and contractile dysfunction, the effects of which were mitigated by CD74 deletion. Furthermore, CD74 knockout reconciled DOX-induced mitochondrial anomalies, apoptosis and ferroptosis. Mechanistically, CD74 directly bound and interacted with RRM2, leading to relocation of RRM2 from cytoplasm to the cytomembrane. As a result, repair of DOX-induced cardiotoxicity was dampened, leading to mitochondrial injury and apoptosis, along activation of the RRM2/p53 cascade, mitochondrial anomalies and ferroptosis. This is supported by the fact that a CD74 mutant deficient in its extracellular domain (aa 220−250) failed to elicit aggravating effects elicited by WT CD74 on DOX-induced cardiac responses. Our observation of a high affinity interaction between the cytoprotective agent Amifostine and CD74 also led to the promises of Amifostine as a therapeutic tool for CD74 inhibition and DIC. Moreover, Amifostine-conferred beneficial effect against DIC was abrogated by p53 activation. These CD74-mediated effects under DOX challenge, *via* RRM2 redistribution, and ferroptosis regulation, drive cardiac remodeling and contractile dysfunction. Collectively, our work, for the first time, identifies CD74 as a key player in the pathogenesis of DIC through mechanisms involving RRM2 redistribution, mitochondrial injury and ferroptosis.

Deranged cardiac geometry and contractile function are well documented in DIC. In our current study, we observed cardiac atrophy, interstitial fibrosis, compromised ejection fraction, fractional shortening, PS and $\pm$ dL/dt, along with increased LVESD and relengthening duration (TR_{90}) in DIC, consistent with our earlier reports[59]. These alterations in cardiac morphology, mechanical properties were accompanied by intracellular Ca^{2+} derangement and oxidative stress, and ferroptosis, suggesting that an essential role for stress signaling in DIC pathology. Especially, DIC was associated with compromised intracellular Ca^{2+} release and delayed intracellular Ca^{2+} clearance, indicating a unique role of intracellular Ca^{2+} dysregulation in the pathogenesis of DIC. Genetic ablation of CD74 conferred protection against DOX-induced cardiac remodeling, contractile dysfunction and intracellular derangement. Along the same line, CD74 knockout mitigated DOX-evoked oxidative stress, apoptosis, ferroptosis, and mitochondrial anomalies, including loss of membrane potential and ultrastructural damage. The cardioprotective effects extended to pharmacological inhibition of CD74 using Amifostine, a cytoprotective agent with high CD74 affinity. This aligns with prior reports of Amifostine's ability to restore mitochondrial function and dampen ROS production in ischemic injury[60]. Importantly, Amifostine's benefits were contingent on CD74-p53 inhibition, as p53 activation nullified its protective effects. These findings position CD74 as a central mediator of DIC pathogenesis and validate its therapeutic targeting.

While our findings support the beneficial effects of Amifostine in DIC through CD74 inhibition, there remains a lack of clinical evidence regarding the utility of antioxidant supplements in DOX-induced heart anomalies. This discrepancy may be due to the less concentrated localization of antioxidants within or near mitochondria and the complex interplay between oxidative stress with other cellular stressors. Our results highlight significant mitochondrial injury in DIC-challenged mouse hearts, as evidenced by disruptions in mitochondrial membrane potential, mitochondrial proteins, and mitochondrial ultrastructure. Previous studies have shown that p53 knockout preserves Cu/Zn superoxide dismutase levels in DOX-treated hearts, implicating p53 in antioxidant

regulation under stressful conditions[61]. In DIC, mitochondrial damage leads to the release of damage-associated molecular patterns (DAMPs), including mtDNA, ATP, and cytochrome *c*, into the cytoplasm and extracellular space. These DAMPs activate pattern recognition receptors (PRRs) on immune cells, triggering an inflammatory response that exacerbates mitochondrial injury[62]. Collectively, the observed mitochondrial damage and apoptosis in DOX-induced cardiotoxicity further underscore the detrimental role of the CD74/RRM2/p53 cascade in DIC.

Ferroptosis has been shown to contribute to the pathogenesis for heart diseases including DIC[12]. Earlier studies demonstrated that inhibition of ferroptosis, rather than other forms of cell death, overtly improved DOX-induced mouse mortality[63,64]. Besides, DOX was shown to decrease cardiac GPX4 expression, resulting in defects in the resistance to lipid peroxidation and onset of ferroptosis[65]. In this context, GPX4 overexpression significantly attenuated DIC *via* inhibition of ferroptosis. Moreover, several medications capable of inhibiting ferroptosis exhibited therapeutic promises in preclinical models of DIC, including dexrazoxane and Fer-1[10]. Therefore, the inhibition of ferroptosis might be a therapeutic strategy against DIC. Here, our findings suggested that genetic ablation and pharmacological inhibition of CD74 overtly suppressed cardiomyocyte ferroptosis in response to DOX treatment.

Although multiple pathologic mechanisms are involved in DIC, limited options are readily available to halt this process. In our hands, we noted a prominent role for RRM2 in DIC. We observed a role for the direct binding of CD74−RRM2 and the downstream activation of p53 in DOX-evoked ferroptosis. Elevated levels of RRM2 are reported in multiple human cancers[65-67]. As such, RRM2 is deemed a diagnostic marker and an established anti-cancer therapeutic target[68,69]. Previous studies have shown that overexpression of RRM2 alleviates DOX-induced cardiac injury by activating AKT/mTOR signaling, which may new therapeutic options for DIC[54]. Our study found that CD74 binds to RRM2 and is transported to the cell membrane to form a complex, mediating apoptosis and ferroptosis. The obligatory role for RRM2 in CD74-associated pathological changes under DOX exposure received validation from the observation that inhibition of RRM2 using GW8510 lessened DOX-instigated cardiac contractile dysfunction. Moreover, p53-induced upregulation in death receptors may also contribute to enhanced cardiomyocyte apoptosis in DIC. Recent evidence also suggests that p53 knockdown in cardiomyocytes can prevent DOX-induced cardiotoxic-related ferroptosis[70]. Future studies are warranted to better discern the role of RRM2 in tumorigenesis and DOX-related heart damage, in particular the involvement of ferroptosis.

Amifostine, sodium diethyldithiocarbamate, is an inactive phosphorylated aminothiol pro-drug and executes its biological action through dephosphorylation to WR-1065, an active and free radical-scavenging sulfhydryl metabolite[71]. Amifostine inhibits bleomycin-induced pulmonary fibrosis by restoring mitochondrial function and cellular metabolism[72]. Amifostine attenuates cardiomyocyte apoptosis and reduces ROS accumulation in I/R challenge, likely through inhibition of cleaved caspase 3 and Bax while enhancing levels of SOD1, SOD2 and Bcl2, to reduce MDA levels[26]. Numerous clinical studies have investigated the use of Amifostine as an adjuvant therapy for gynecological, colorectal, and head tumors. Combined with our findings, this information suggests that Amifostine may emerge as a new therapeutic option for cardiac protection against DOX-induced heart damage.

Our Transwell co-culture study using CD74-deficient RAW 264.7 macrophages and AMCMs demonstrated that CD74 knockdown specifically in macrophages markedly alleviated DOX-induced cardiomyocyte dysfunction and inflammatory markers in medium, highlighting a critical role of macrophages (and release proinflammatory cytokines IL-6, IL-1β, and TNF-α) in CD74 ablation-elicited cardioprotection against DIC. CD74 is known to exhibit diverse functions depending on the context of disease, cell type, and its downstream signaling[19,20]. In the setting of DIC, mounting evidence indicates that proinflammatory cytokines significantly contributes to myocardial injury in addition to oxidative stress and mitochondrial damage[1,3]. Our findings further support this, showing that CD74 deficiency in macrophages suppresses secretion of inflammatory cytokines, in turn alleviating cardiomyocyte contractile dysfunction. These results suggest that the DIC pathogenesis is, at least in part, dependent on macrophage-mediated inflammatory responses, and that targeting CD74 in macrophages may represent a promising strategy for cardioprotection.

Experimental limitation: several limitations exist in this study. First, although DIC primarily affects women and is closely associated with a higher incidence of breast cancer, we only used male mice for our animal study, which is inconsistent with the human disease profile. Future studies should investigate potential sex differences in the CD74-mediated response in DOX-induced cardiomyopathy to better align with the human condition. Next, acute *in vitro* DOX exposure cannot fully replicate chronic DOX-induced cardiac changes, although our past studies show that this model effectively captures many *in vivo* alterations[40,73,74]. Additionally, it enables direct assessment of DOX, Amifostine, and anti-ferroptotic drugs on cardiomyocytes, independent of other cell types. Despite the apparent limitations, the *in vitro* system remains a valuable tool for studying cell signaling mechanisms.

5. Conclusions

In summary, our findings suggest that CD74 ablation or inhibition using Amifostine alleviates DOX-induced cardiac remodeling and contractile anomalies by mitigating oxidative stress and ferroptosis. Our results further indicated a seemingly vital role for macrophages and secretion of inflammatory cytokines in CD74 deletion-elicited cardioprotection in the face of DOX cardiotoxicity. These results support the notion that ferroptosis acts as a final instigator for this pathological process, likely downstream of oxidative stress, in DOX-evoked cardiac morphological and functional anomalies. These findings should provide new insights into the role of ferroptosis in DOX-induced mitochondrial injury and cardiomyopathy (Fig. 8S). While previous evidence has highlighted a prominent role for oxidative stress in DIC[75-78], the poor translation of antioxidant therapy in the management of DOX-induced organ complications may be due to the complex interplay of oxidative stress with other cell death processes. Future work is necessary to further elucidate the intricate relationship between oxidative stress and ferroptosis in DOX-induced cardiac anomalies.

Acknowledgments

We would like to thank Dr Yu Kong and Xu Wang (Electron Microscopy Facilities of the Center for Excellence in Brain Science and Technology, Chinese Academy of Science) for assistance with EM sample preparation and EM image analysis. This study was sponsored by Shanghai Xuhui Healthcare System Peak Discipline Construction Funding Project (No. SHXHZDXK202305, China), Open Research (No. 09, China)

Fund of State Key Laboratory of Cardiovascular Diseases, National Basic Research Center of China (T2288101), National Natural Science Foundation of China (82130011), Shanghai Top Priority Research Center Construction Project (2022ZZ01010, China), and the National Science Fund for Distinguished Young Scholars (82425005, China).

Author contributions

Miyesaier Abudureyimu drafted the manuscript. Guizhen Wang, Xing Qin, and Peizhi Miao provided helpful comments. Jie Qi, Richard Bucala, and Rong Chen provided resources for the study. Miyesaier Abudureyimu, Junbo Ge, and Yingmei Zhang conceived and designed the study, and Xuanming Luo and Jun Ren edited and proved the manuscript.

Conflicts of interest

The authors declare no conflicts of interest.

Appendix A. Supporting information

Supporting information to this article can be found online at https://doi.org/10.1016/j.apsb.2026.01.028.

References

1. Wenningmann N, Knapp M, Ande A, Vaidya TR, Ait-Oudhia S. Insights into Doxorubicin-induced cardiotoxicity: molecular mechanisms, preventive strategies, and early monitoring. *Mol Pharmacol* 2019;**96**:219−32.
2. Shafei A, El-Bakly W, Sobhy A, Wagdy O, Reda A, Aboelenin O, et al. A review on the efficacy and toxicity of different doxorubicin nanoparticles for targeted therapy in metastatic breast cancer. *Biomed Pharmacother* 2017;**95**:1209−18.
3. Sumneang N, Tanajak P, Oo TT. Toll-like receptor 4 inflammatory perspective on Doxorubicin-induced cardiotoxicity. *Molecules* 2023; **28**:4294.
4. Haesen S, Jager MM, Brillouet A, de Laat I, Vastmans L, Verghote E, et al. Pyridoxamine limits cardiac dysfunction in a rat model of doxorubicin-induced cardiotoxicity. *Antioxidants* 2024;**13**:112.
5. Kitakata H, Endo J, Ikura H, Moriyama H, Shirakawa K, Katsumata Y, et al. Therapeutic targets for DOX-induced cardiomyopathy: role of apoptosis *vs*. ferroptosis. *Int J Mol Sci* 2022;**23**:1414.
6. Bartlett JJ, Trivedi PC, Pulinilkunnil T. Autophagic dysregulation in doxorubicin cardiomyopathy. *J Mol Cell Cardiol* 2017;**104**:1−8.
7. Wu L, Wang L, Du Y, Zhang Y, Ren J. Mitochondrial quality control mechanisms as therapeutic targets in doxorubicin-induced cardiotoxicity. *Trends Pharmacol Sci* 2023;**44**:34−49.
8. Wu L, Zhang Y, Wang G, Ren J. Molecular mechanisms and therapeutic targeting of ferroptosis in doxorubicin-induced cardiotoxicity. *JACC Basic Transl Sci* 2024;**9**:811−26.
9. Wu L, Du Y, Wang L, Zhang Y, Ren J. Inhibition of METTL3 ameliorates doxorubicin-induced cardiotoxicity through suppression of TFRC-mediated ferroptosis. *Redox Biol* 2024;**72**:103157.
10. Fang X, Wang H, Han D, Xie E, Yang X, Wei J, et al. Ferroptosis as a target for protection against cardiomyopathy. *Proc Natl Acad Sci U S A* 2019;**116**:2672−80.
11. Qiu H, Huang S, Liu Y, Liu L, Guo F, Guo Y, et al. Idebenone alleviates doxorubicin-induced cardiotoxicity by stabilizing FSP1 to inhibit ferroptosis. *Acta Pharm Sin B* 2024;**14**:2581−97.
12. Tadokoro T, Ikeda M, Ide T, Deguchi H, Ikeda S, Okabe K, et al. Mitochondria-dependent ferroptosis plays a pivotal role in doxorubicin cardiotoxicity. *JCI Insight* 2020;**5**:e132747.
13. Bonnin E, Rodrigo Riestra M, Marziali F, Mena Osuna R, Denizeau J, Maurin M, et al. CD74 supports accumulation and function of regulatory T cells in tumors. *Nat Commun* 2024;**15**:3749.
14. Ghoochani A, Schwarz MA, Yakubov E, Engelhorn T, Doerfler A, Buchfelder M, et al. MIF−CD74 signaling impedes microglial M1 polarization and facilitates brain tumorigenesis. *Oncogene* 2016;**35**: 6246−61.
15. Farr L, Ghosh S, Moonah S. Role of MIF Cytokine/CD74 receptor pathway in protecting against injury and promoting repair. *Front Immunol* 2020;**11**:1273.
16. De R, Sarkar S, Mazumder S, Debsharma S, Siddiqui AA, Saha SJ, et al. Macrophage migration inhibitory factor regulates mitochondrial dynamics and cell growth of human cancer cell lines through CD74−NF-κB signaling. *J Biol Chem* 2018;**293**:19740−60.
17. Gore Y, Starlets D, Maharshak N, Becker-Herman S, Kaneyuki U, Leng L, et al. Macrophage migration inhibitory factor induces B cell survival by activation of a CD74−CD44 receptor complex. *J Biol Chem* 2008;**283**:2784−92.
18. Farr L, Ghosh S, Jiang N, Watanabe K, Parlak M, Bucala R, et al. CD74 signaling links inflammation to intestinal epithelial cell regeneration and promotes mucosal healing. *Cell Mol Gastroenterol Hepatol* 2020;**10**:101−12.
19. Zhang L, Woltering I, Holzner M, Brandhofer M, Schaefer CC, Bushati G, et al. CD74 is a functional MIF receptor on activated $CD4^+$ T cells. *Cell Mol Life Sci* 2024;**81**:296.
20. Li QL, Tang J, Zhao L, Ruze A, Shan XF, Gao XM. The role of CD74 in cardiovascular disease. *Front Cardiovasc Med* 2022;**9**:1049143.
21. Wu BB, Leung KT, Poon EN. Mitochondrial-targeted therapy for doxorubicin-induced cardiotoxicity. *Int J Mol Sci* 2022;**23**:1912.
22. Wang Y, Yan S, Liu X, Deng F, Wang P, Yang L, et al. PRMT4 promotes ferroptosis to aggravate doxorubicin-induced cardiomyopathy *via* inhibition of the Nrf2/GPX4 pathway. *Cell Death Differ* 2022; **29**:1982−95.
23. Alizadeh D, Trad M, Hanke NT, Larmonier CB, Janikashvili N, Bonnotte B, et al. Doxorubicin eliminates myeloid-derived suppressor cells and enhances the efficacy of adoptive T-cell transfer in breast cancer. *Cancer Res* 2014;**74**:104−18.
24. Ritchie ME, Phipson B, Wu D, Hu Y, Law CW, Shi W, et al. Limma powers differential expression analyses for RNA-sequencing and microarray studies. *Nucleic Acids Res* 2015;**43**:e47.
25. Li DL, Wang ZV, Ding G, Tan W, Luo X, Criollo A, et al. Doxorubicin blocks cardiomyocyte autophagic flux by inhibiting lysosome acidification. *Circulation* 2016;**133**:1668−87.
26. Wu SZ, Tao LY, Wang JN, Xu ZQ, Wang J, Xue YJ, et al. Amifostine pretreatment attenuates myocardial ischemia/reperfusion injury by inhibiting apoptosis and oxidative stress. *Oxid Med Cell Longev* 2017; **2017**:4130824.
27. Hum NR, Sebastian A, Martin KA, Rios-Arce ND, Gilmore SF, Gravano DM, et al. IL-17A increases doxorubicin efficacy in triple negative breast cancer. *Front Oncol* 2022;**12**:928474.
28. Naso FD, Bruqi K, Manzini V, Chiurchiù V, D'Onofrio M, Arisi I, et al. miR-218-5p and doxorubicin combination enhances anticancer activity in breast cancer cells through Parkin-dependent mitophagy inhibition. *Cell Death Discov* 2024;**10**:149.
29. Chen S, Chen J, Du W, Mickelsen DM, Shi H, Yu H, et al. PDE10A inactivation prevents doxorubicin-induced cardiotoxicity and tumor growth. *Circ Res* 2023;**133**:138−57.
30. Li W, Sultana N, Yuan L, Forssell C, Yuan XM. CD74 in apoptotic macrophages is associated with inflammation, plaque progression and clinical manifestations in human atherosclerotic lesions. *Metabolites* 2022;**12**:54.
31. Cox CB, Castro M, Brown TL, Bigley NJ. IL-10 and TGF-β increase connexin-43 expression and membrane potential of HL-1 cardiomyocytes coupled with RAW 264.7 macrophages. *Immunohorizons* 2022;**6**:334−43.
32. Jones SP, Zachara NE, Ngoh GA, Hill BG, Teshima Y, Bhatnagar A, et al. Cardioprotection by *N*-acetylglucosamine linkage to cellular proteins. *Circulation* 2008;**117**:1172−82.

33. Liu Q, Dong Y, Escames G, Wu X, Ren J, Yang W, et al. Identification of PIK3CG as a hub in septic myocardial injury using network pharmacology and weighted gene co-expression network analysis. *Bioeng Transl Med* 2023;**8**:e10384.
34. Min J, Wu L, Liu Y, Song G, Deng Q, Jin W, et al. Empagliflozin attenuates trastuzumab-induced cardiotoxicity through suppression of DNA damage and ferroptosis. *Life Sci* 2023;**312**:121207.
35. Strom E, Sathe S, Komarov PG, Chernova OB, Pavlovska I, Shyshynova I, et al. Small-molecule inhibitor of p53 binding to mitochondria protects mice from gamma radiation. *Nat Chem Biol* 2006;**2**:474−9.
36. Napolitano R, De Matteis S, Carloni S, Bruno S, Abbati G, Capelli L, et al. Kevetrin induces apoptosis in TP53 wild-type and mutant acute myeloid leukemia cells. *Oncol Rep* 2020;**44**:1561−73.
37. Hsieh YY, Chou CJ, Lo HL, Yang PM. Repositioning of a cyclin-dependent kinase inhibitor GW8510 as a ribonucleotide reductase M2 inhibitor to treat human colorectal cancer. *Cell Death Discov* 2016;**2**:16027.
38. Maurya SK, Carley AN, Maurya CK, Lewandowski ED. Western diet causes heart failure with reduced ejection fraction and metabolic shifts after diastolic dysfunction and novel cardiac lipid derangements. *JACC Basic Transl Sci* 2023;**8**:422−35.
39. Xu H, Yu W, Sun S, Li C, Zhang Y, Ren J. Luteolin attenuates doxorubicin-induced cardiotoxicity through promoting mitochondrial autophagy. *Front Physiol* 2020;**11**:113.
40. Liu Y, Shen M, Zhu S, Du Z, Lin L, Ma J, et al. Metallothionein rescues doxorubicin cardiomyopathy *via* mitigation of cuproptosis. *Life Sci* 2025;**363**:123379.
41. Chen L, Yin Z, Qin X, Zhu X, Chen X, Ding G, et al. CD74 ablation rescues type 2 diabetes mellitus-induced cardiac remodeling and contractile dysfunction through pyroptosis-evoked regulation of ferroptosis. *Pharmacol Res* 2022;**176**:106086.
42. Yang M, Wang S, Fu S, Wu NN, Xu X, Sun S, et al. Deletion of the E3 ubiquitin ligase, Parkin, exacerbates chronic alcohol intake-induced cardiomyopathy through an Ambra1-dependent mechanism. *Br J Pharmacol* 2021;**178**:964−82.
43. Ren J, Sun M, Zhou H, Ajoolabady A, Zhou Y, Tao J, et al. FUNDC1 interacts with FBXL2 to govern mitochondrial integrity and cardiac function through an IP3R3-dependent manner in obesity. *Sci Adv* 2020;**6**:eabc8561.
44. Van den Bos EJ, Wagner A, Mahrholdt H, Thompson RB, Morimoto Y, Sutton BS, et al. Improved efficacy of stem cell labeling for magnetic resonance imaging studies by the use of cationic liposomes. *Cell Transplant* 2003;**12**:743−56.
45. Garrido-Jareño M, Puchades-Carrasco L, Orti-Pérez L, Sahuquillo-Arce JM, Del Carmen Meyer-García M, Mollar-Maseres J, et al. A surface plasmon resonance based approach for measuring response to pneumococcal vaccine. *Sci Rep* 2021;**11**:6502.
46. Bi Y, Liu S, Qin X, Abudureyimu M, Wang L, Zou R, et al. FUNDC1 interacts with GPx4 to govern hepatic ferroptosis and fibrotic injury through a mitophagy-dependent manner. *J Adv Res* 2024;**55**:45−60.
47. Wei C, Shi M, Dong S, Li Z, Zhao B, Liu D, et al. SIRT5-related lysine demalonylation of GSTP1 contributes to cardiomyocyte pyroptosis suppression in diabetic cardiomyopathy. *Int J Biol Sci* 2024;**20**:585−605.
48. Bayer AL, Zambrano MA, Smolgovsky S, Robbe ZL, Ariza A, Kaur K, et al. Cytotoxic T cells drive doxorubicin-induced cardiac fibrosis and systolic dysfunction. *Nat Cardiovasc Res* 2024;**3**:970−86.
49. David K, Friedlander G, Pellegrino B, Radomir L, Lewinsky H, Leng L, et al. CD74 as a regulator of transcription in normal B cells. *Cell Rep* 2022;**41**:111572.
50. Westmeier J, Brochtrup A, Paniskaki K, Karakoese Z, Werner T, Sutter K, et al. Macrophage migration inhibitory factor receptor CD74 expression is associated with expansion and differentiation of effector T cells in COVID-19 patients. *Front Immunol* 2023;**14**:1236374.
51. Shu Z, Li Z, Huang H, Chen Y, Fan J, Yu L, et al. Cell-cycle-dependent phosphorylation of RRM1 ensures efficient DNA replication and regulates cancer vulnerability to ATR inhibition. *Oncogene* 2020;**39**:5721−33.
52. Chen E, Widjaja V, Kyro G, Allen B, Das P, Prahaladan VM, et al. Mapping N- to C-terminal allosteric coupling through disruption of a putative CD74 activation site in D-dopachrome tautomerase. *J Biol Chem* 2023;**299**:104729.
53. Wang R, Xu Z, Tian J, Liu Q, Dong J, Guo L, et al. Pterostilbene inhibits hepatocellular carcinoma proliferation and HBV replication by targeting ribonucleotide reductase M2 protein. *Am J Cancer Res* 2021;**11**:2975−89.
54. Jiao Y, Li Y, Zhang J, Zhang S, Zha Y, Wang J. RRM2 Alleviates doxorubicin-induced cardiotoxicity through the AKT/mTOR signaling pathway. *Biomolecules* 2022;**12**:299.
55. Vaddavalli PL, Schumacher B. The p53 network: cellular and systemic DNA damage responses in cancer and aging. *Trends Genet* 2022;**38**:598−612.
56. Peuget S, Zhou X, Selivanova G. Translating p53-based therapies for cancer into the clinic. *Nat Rev Cancer* 2024;**24**:192−215.
57. Spencer CM, Goa KL. Amifostine. A review of its pharmacodynamic and pharmacokinetic properties, and therapeutic potential as a radioprotector and cytotoxic chemoprotector. *Drugs* 1995;**50**:1001−31.
58. Culy CR, Spencer CM. Amifostine: an update on its clinical status as a cytoprotectant in patients with cancer receiving chemotherapy or radiotherapy and its potential therapeutic application in myelodysplastic syndrome. *Drugs* 2001;**61**:641−84.
59. Bi Y, Xu H, Wang X, Zhu H, Ge J, Ren J, et al. FUNDC1 protects against doxorubicin-induced cardiomyocyte PANoptosis through stabilizing mtDNA *via* interaction with TUFM. *Cell Death Dis* 2022;**13**:1020.
60. Cheng H, Lv M, Mi R, Xue G. Amifostine ameliorates cerebral ischaemia−reperfusion injury *via* p38-mediated oxidative stress and mitochondrial dysfunction. *Folia Neuropathol* 2020;**58**:334−46.
61. Shizukuda Y, Matoba S, Mian OY, Nguyen T, Hwang PM. Targeted disruption of p53 attenuates doxorubicin-induced cardiac toxicity in mice. *Mol Cell Biochem* 2005;**273**:25−32.
62. Zha W, Zhao Q, Xiao Y, Gan Y, Wei J, Yu M, et al. Mitochonic acid 5 rescues cardiomyocytes from doxorubicin-induced toxicity *via* repressing the TNF-α/NF-κB/NLRP3-mediated pyroptosis. *Int Immunopharmacol* 2023;**123**:110736.
63. Fang X, Cai Z, Wang H, Han D, Cheng Q, Zhang P, et al. Loss of cardiac ferritin H facilitates cardiomyopathy *via* Slc7a11-mediated ferroptosis. *Circ Res* 2020;**127**:486−501.
64. Huang C, Guo Y, Li T, Sun G, Yang J, Wang Y, et al. Pharmacological activation of GPX4 ameliorates doxorubicin-induced cardiomyopathy. *Redox Biol* 2024;**70**:103024.
65. Cheng B, Li L, Wu Y, Luo T, Tang C, Wang Q, et al. The key cellular senescence related molecule RRM2 regulates prostate cancer progression and resistance to docetaxel treatment. *Cell Biosci* 2023;**13**:211.
66. Xiong W, Zhang B, Yu H, Zhu L, Yi L, Jin X. RRM2 regulates sensitivity to sunitinib and PD-1 blockade in renal cancer by stabilizing ANXA1 and activating the AKT pathway. *Adv Sci (Weinh)* 2021;**8**:e2100881.
67. Khan P, Siddiqui JA, Kshirsagar PG, Venkata RC, Maurya SK, Mirzapoiazova T, et al. MicroRNA-1 attenuates the growth and metastasis of small cell lung cancer through CXCR4/FOXM1/RRM2 axis. *Mol Cancer* 2023;**22**:1.
68. Zheng S, Wang X, Weng YH, Jin X, Ji JL, Guo L, et al. siRNA Knockdown of RRM2 effectively suppressed pancreatic tumor growth alone or synergistically with doxorubicin. *Mol Ther Nucleic Acids* 2018;**12**:805−16.
69. Morikawa T, Maeda D, Kume H, Homma Y, Fukayama M. Ribonucleotide reductase M2 subunit is a novel diagnostic marker and a potential therapeutic target in bladder cancer. *Histopathology* 2010;**57**:885−92.
70. Pan J, Xiong W, Zhang A, Zhang H, Lin H, Gao L, et al. The imbalance of p53−Park7 signaling axis induces iron homeostasis dysfunction in doxorubicin-challenged cardiomyocytes. *Adv Sci (Weinh)* 2023;**10**:e2206007.

71. Singh VK, Seed TM. The efficacy and safety of amifostine for the acute radiation syndrome. *Expet Opin Drug Saf* 2019;**18**:1077−90.
72. Guo F, Xu F, Li S, Zhang Y, Lv D, Zheng L, et al. Amifostine ameliorates bleomycin-induced murine pulmonary fibrosis *via* NAD^+/SIRT1/AMPK pathway-mediated effects on mitochondrial function and cellular metabolism. *Eur J Med Res* 2024;**29**:68.
73. Ren J, Wold LE. Measurement of cardiac mechanical function in isolated ventricular myocytes from rats and mice by computerized video-based imaging. *Biol Proced Online* 2001;**3**:43−53.
74. Yu W, Qin X, Zhang Y, Qiu P, Wang L, Zha W, et al. Curcumin suppresses doxorubicin-induced cardiomyocyte pyroptosis *via* a PI3K/Akt/mTOR-dependent manner. *Cardiovasc Diagn Ther* 2020;**10**: 752−69.
75. Jiang S, Zhu W, Li C, Zhang X, Lu T, Ding Z, et al. Alpha-lipoic acid attenuates LPS-induced cardiac dysfunction through a PI3K/Akt-dependent mechanism. *Int Immunopharmacol* 2013;**16**:100−7.
76. Singh J, Lee Y, Kellum JA. A new perspective on NO pathway in sepsis and ADMA lowering as a potential therapeutic approach. *Crit Care* 2022;**26**:246.
77. Zapelini PH, Rezin GT, Cardoso MR, Ritter C, Klamt F, Moreira JC, et al. Antioxidant treatment reverses mitochondrial dysfunction in a sepsis animal model. *Mitochondrion* 2008;**8**:211−8.
78. Zhao P, Turdi S, Dong F, Xiao X, Su G, Zhu X, et al. Cardiac-specific overexpression of insulin-like growth factor I (IGF-1) rescues lipopolysaccharide-induced cardiac dysfunction and activation of stress signaling in murine cardiomyocytes. *Shock* 2009;**32**:100−7.